博士論文

Studies on the intraorganelle environment
in magnetotactic bacterium
Magnetospirillum magneticum AMB-1

（和訳）磁性細菌 *Magnetospirillum magneticum*
AMB-1 の
オルガネラ内部環境に関する研究

金沢大学大学院自然科学研究科
生命科学専攻
動態生理学講座

学　籍　番　号　　　　　　1323032004
氏　　　　　　名　　　　　江口　友佳子
主任指導教官氏名　　　　　　田岡　東
提出年月　　　　　平成 30 年 1 月 5 日

CONTENTS

Abbreviations

AMB-1	*Magnetospirillum magneticum* AMB-1
ATCC	American Type Culture Collection
CCCP	Carbonyl cyanide *m*-chlorophenyl hydrazine
Ccm	Cytochrome *c* maturation
CDF	Cation diffusion facilitator
DAP	2, 6-Diaminopimelic acid
IgG	immunoglobulin G
kDa	kilo Dalton or 1000 dalton
LB medium	Luria-Bertani medium
MAI	Magnetosome island
MSGM	magnetic spirillum growth medium
Mob	Relaxase for conjugal plasmid transfer
OD	Optical density
PBS	Phosphate buffered saline
PCR	Polymerase chain reaction
PVDF	Polyvinylidene difluoride
SDS-PAGE	Sodium dodecyl sulfate polyacrylamide gel electrophoresis
Tat	Twin-arginine translocation
TEM	Transmission electron microscopy
Tris	tris (hysroxymethyl) aminomethane
WT	*Magnetospirillum magneticum* AMB-1 of wild type

Chapter I

General Introduction

Magnetotactic bacteria

Magnetotactic bacteria are ubiquitous aquatic eubacteria that possess the ability to navigate along the Earth's magnetic field for reaching their favorable microaerobic habitat (Uebe & Schüler, 2016). The unique capability to sense magnetic fields relies on "magnetosomes" which are biotically synthesized magnetic nanoparticles enveloped with phospholipid bilayer vesicles (Fig. 1-1). Owing to the universality and specificity in interesting properties of magnetotactic bacteria including magnetic sensing, magnetosome formation, and biomineralization, they have attracted much interest from various academic disciplines. In Chapter I, I will summarize elementary knowledge of magnetotactic bacteria.

Magnetotactic bacteria have a worldwide geographical distribution, and inhabit sediments of aquatic environments including fresh, marine, brackish, hypersaline, and chemically stratified water (Lefèvre & Bazylinski, 2013). In contrast to the broad horizontal distribution, the vertical distribution of magnetotactic bacteria is restricted by oxygen concentration responsible for availability of reduced compounds such as Fe^{2+} and hydrogen sulfide (Flies et al., 2005). Most magnetotactic bacteria occur in aquatic habitats at mesothermal temperature and neutral pH. On the other hand, some extremophilic magnetotactic bacteria were found in hot springs (Lefèvre et al., 2010) and alkaline lakes (Lefèvre et al., 2011). Due to the presence of moderately thermophilic and alkaliphilic magnetotactic bacteria, it should be not unreasonable that other extremophilic magnetotactic bacteria exist.

Magnetotactic bacteria are a phylogenetically diverse group of Gram-negative

bacteria. Known magnetotactic bacteria belong to different *Proteobacteria* phylum subgroups, including at least *alpha-*, *gamma-*, and *delta-*subgroups; the *Nitrospirae* phylum; and the OP3 of the PVC (*Planctomycetes*, *Verrucomicrobia*, and *Chlamydiae*) superphylum (Lefèvre & Bazylinski, 2013). Thus, magnetotactic bacteria do not form a phylogenetically coherent group.

Magneto-aerotaxis

Magnetotaxis is considered to assist in confining within the microaerobic zone located in chemically stratified basins or sediments (Frankel et al., 1997). The intracellular magnetic dipoles of magnetosomes allow to swim along the geomagnetic field (Fig. 1-2). Owing to the inclination of the geomagnetic field, magnetotactic bacteria swim unidirectionally along the vertical axis in aquatic environments. In the Northern Hemisphere, the majority of magnetotactic bacterial population shows north-seeking directivity (swimming toward the magnetic S-pole). While, that in the Southern Hemisphere shows south-seeking directivity (swimming toward the magnetic N-pole), opposing to the Northern Hemisphere. In addition, magnetotactic bacterial population at the equator, where the geomagnetic field is nearly horizontal, display no bias between north-seeking and south-seeking directivity (Blakemore 1975; Blakemore 1982). Therefore, magnetotactic bacteria in both the Northern Hemisphere and the Southern Hemisphere swim toward the bottom of water where the oxygen concentration is lower than the surface. Therefore, the combination of magnetotaxis and aerotaxis, termed "magneto-aerotaxis," facilitates magnetotactic bacteria to migrate to microaerobic zone. (Frankel et al., 1997).

Structure of magnetosome

Magnetosomes are highly organized structure to function as a magnetic sensor. Magnetosomes consist of regular-sized magnetite or greigite nanocrystals enveloped with phospholipid bilayer membrane and magnetosome-associated proteins. In a magnetotactic bacterial cell, magnetosomes are arranged in one or multiple chains along the cell length.

The observations using cryo-electron tomography revealed *in situ* ultrastructure of magnetosomes (Komeili et al., 2006; Scheffel et al., 2006). Figure 1-3 shows schematics of the magnetosome structures. According to these observations, magnetosome vesicles are aligned along networks of filamentous structures. These filaments appeared to be comprised of MamK, a bacterial homolog of actin, based on the phenotype of the *mamK* deletion mutant (Komeili et al., 2006; Scheffel et al., 2006). Moreover, it was suggested that MamK cytoskeletal filaments maintains the chain structure of magnetosomes during the cell cycle, for *mamK* deletion resulted in dispersion of magnetosomes within cells (Taoka et al., 2017). Chain alignment of magnetosomes contributes to gain enough magnetic moments to orient a cell along the geomagnetic field. Furthermore, it was suggested that magnetosome vesicles resulted from the invagination of cytoplasmic membrane because all magnetosomes, including empty vesicles, were continuous to the cytoplasmic membrane via narrow constrictions. The access between magnetosomes and the periplasm might allow for transport of small molecules required to synthesize magnetite crystals.

Magnetosome-associated proteins and magnetosome island

Although magnetosome vesicles are derived from the cytoplasmic membrane,

magnetosome vesicles contain specific proteins distinct from the cytoplasmic membrane (Gorby et al., 1988; Okuda et al., 1996). The proteomic analysis of isolated magnetosomes uncovered various features of magnetosome-associated proteins, such as tetratricopeptide repeat (TPR) proteins, cytoskeletal proteins, cation diffusion facilitators (CDF), serine proteases, heme *c* binding proteins and hypothetical proteins (Grünberg et al., 2004). Interestingly, genes encoding magnetosome-associated proteins are assembled in a specific genomic region called magnetosome island (MAI) (Shübbe et al., 2003; Ullrich et al., 2005). A typical MAI consists of four core operons: *mamGFDC, mms6, mamAB* and *mamXY* operons (Fig 1-4). The proteins encoded in MAI display no significant homology to proteins encoded in non-magnetotactic bacteria, thus they seem to function specifically for magnetosome.

Formation of magnetosome

Although the detailed process of magnetosome formation remains unclear, the following proposed processes are generally accepted (Uebe & Schüler 2016) (Fig. 1-5). First, magnetosome vesicles are formed throughout the cell by invagination of the cytoplasmic membrane. Second, iron is transported from the cytoplasm into the magnetosome vesicle by iron transporters localized in the magnetosome membrane. Third, a single magnetite crystal is nucleated in the magnetosome lumen; then, a regular-shaped cuboctahedral magnetite crystal is grown until it reaches approximately 50 nm in diameter.

It has been clarified that each of these steps is precisely controlled by the genes in MAI. A spontaneous deletion of the MAI included the *mamAB, mms6 and mamGFDC*

operons caused an inability to form magnetosomes (Ullrich et al., 2010). Furthermore, the gene deletion analysis of the MAI in *M. magneticum* AMB-1 revealed that the *mamAB* operon are essential for magnetosome formation, whereas the deletion of the gene regions including parts of the *mamGFDC* and *mms6* operons led to severe defects in the size and morphology of the crystals (Murat et al., 2010). This suggested that the *mamAB* operon may contain the minimum genes to form magnetosomes (Murat et al., 2010).

Magnetite crystals biomineralized in magnetotactic bacteria have remarkable features: homogeneity in size and morphology, and single magnetic domain structure, ensuring high performance of magnetosomes as magnetic sensors. Magnetite biomineralization requires several processes including iron uptake from the external environments, transport of iron into magnetosome vesicle, magnetite crystal nucleation and crystal growth (Fig. 1-5). However, the detailed mechanism underlying magnetite crystal formation in the magentosome vesicle remains unclear. The internal environment of the magnetosome, including pH and redox potential, should be well-controlled for the synthesis of a magnetite crystal. However, no study has reported the evaluation of the magnetosome lumen environment.

References

Blakemore RP. (1975) Magnetotactic bacteria. *Science.* 190:377-379

Blakemore RP. (1982) Magnetotactic bacteria. *Annu Rev Microbiol.* 36:217-238.

Flies CB, Peplies J, Schüler D. (2005) Combined approach for characterization of uncultivated magnetotactic bacteria from various aquatic environments. *Appl Environ Microbiol.* 71:2723-2731.

Frankel RB, Bazylinski DA, Johnson MS, Taylor BL, (1997) Magneto-aerotaxis in marine coccoid bacteria. *Biophys J.* 73:994-1000

Gorby YA, Beveridge TJ, Blakemore RP. (1988) Characterization of bacterial magnetosome membrane. *J Bacteriol.* 170, 834-841.

Grünberg K, Müller EC, Otto Reszka R, Linder D, Kube M, Reinhardt R, Schüler D. (2004) Biochemical and proteomic analysis of the magnetosome membrane in *Magnetospirillum gryphiswaldense*. *Appl Environ Microbiol.* 70:1040-1050.

Komeili A, Li Z, Newman DK, Jensen GJ. (2006) Magnetosomes are cell membrane invaginations organized by the actin-like protein MamK. *Science.* 311:242-245.

Lefèvre CT, Abreu F, Schmidt ML, Lins U, Frankel RB, Hedlund BP, Bazylinski DA. (2010) Moderately thermophilic magnetotactic bacteria from hot springs in Nevada. *Appl Environ Microbiol.* 76:3740-3743.

Lefèvre CT, Bazylinski DA. (2013) Ecology, diversity, and evolution of magnetotactic

bacteria. *Microbiol Mol Biol Rev.* 77:497-526.

Lefèvre CT, Frankel RB, Pósfai M, Prozorov T, Bazylinski DA. (2011) Isolation of obligately alkaliphilic magnetotactic bacteria from extremely alkaline environments. *Environ Microbiol.* 13:2342-2350.

Murat D, Quinlan A, Vali H, Komeili A. (2010) Comprehensive genetic dissection of the magnetosome gene island reveals the step-wise assembly of a prokaryotic organelle. *Proc Natl Acad Sci USA.* 107:5593-5598.

Okuda Y, Denda K, Fukumori Y. (1996) Cloning and sequencing of a gene encoding a new member of the tetratricopeptide protein family from magnetosomes of *Magnetospirillum magnetotacticum. Gene.* 171:99-102.

Richter M, Kube M, Bazylinski DA, Lombardot T, Glöckner FO, Reinhardt R, Schüler D. (2007) Comparative genome analysis of four magnetotactic bacteria reveals a complex set of group-specific genes implicated in magnetosome biomineralization and function. *J Bacteriol.* 189:4899-4910.

Scheffel A, Gruska M, Faivre D, Linaroudis A, Plitzko JM, Schüler D. (2006) An acidic protein aligns magnetosomes along a filamentous structure in magnetotactic bacteria. *Nature.* 440:110-114.

Schübbe S, Kube M, Scheffel A, Wawer C, Heyen U, Meyerdierks A, Madkour MH, Mayer F, Reinhardt R, Schüler D. (2003) Characterization of a spontaneous nonmagnetic mutant of *Magnetospirillum gryphiswaldense* reveals a large deletion comprising a putative

magnetosome island. *J Bacteriol.* 185:5779-5790.

Taoka A, Kiyokawa A, Uesugi C, Kikuchi Y, Oestreicher Z, Morii K, Eguchi Y, Fukumori Y. (2017) Tethered magnets are the key to magnetotaxis: direct observations of *Magnetospirillum magneticum* AMB-1 show that MamK distributes magnetosome organelles equally to daughter cells. *mBio*. 8: e00679-17.

Ullrich S, Kube M, Schübbe S, Reinhardt R, Schüler D. (2005) A hypervariable 130-kilobase genomic region of *Magnetospirillum gryphiswaldense* comprises a magnetosome island which undergoes frequent rearrangements during stationary growth. *J Bacteriol.* 187:7176-7184.

Uebe R, Schüler D. (2016) Magnetosome biogenesis in magnetotactic bacteria. *Nat Rev Microbiol.* 14:621-637.

Figures
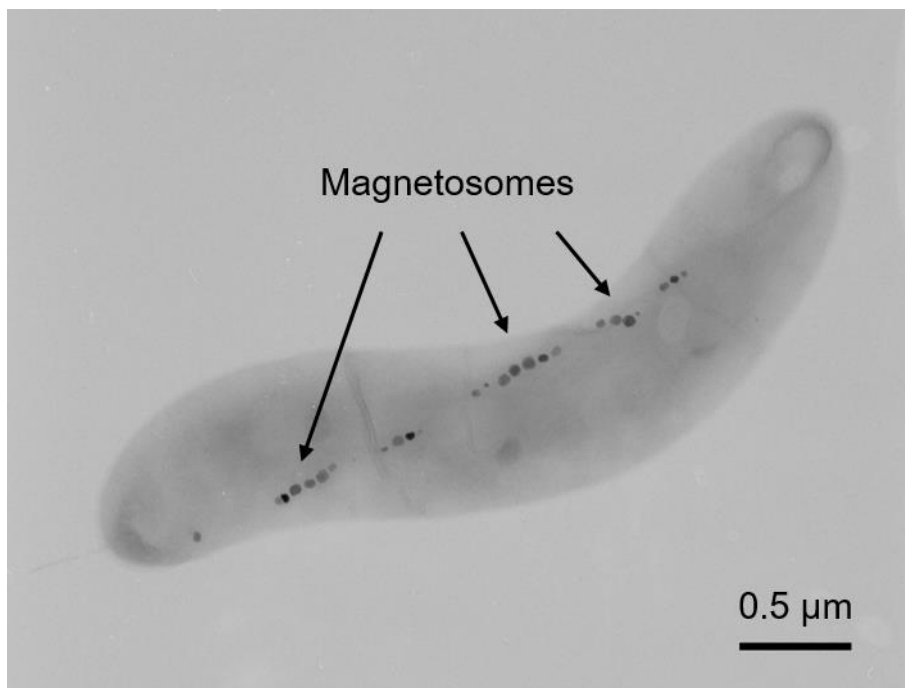
Fig. 1-1 Transmission electron microscopic images of magnetotactic bacterium

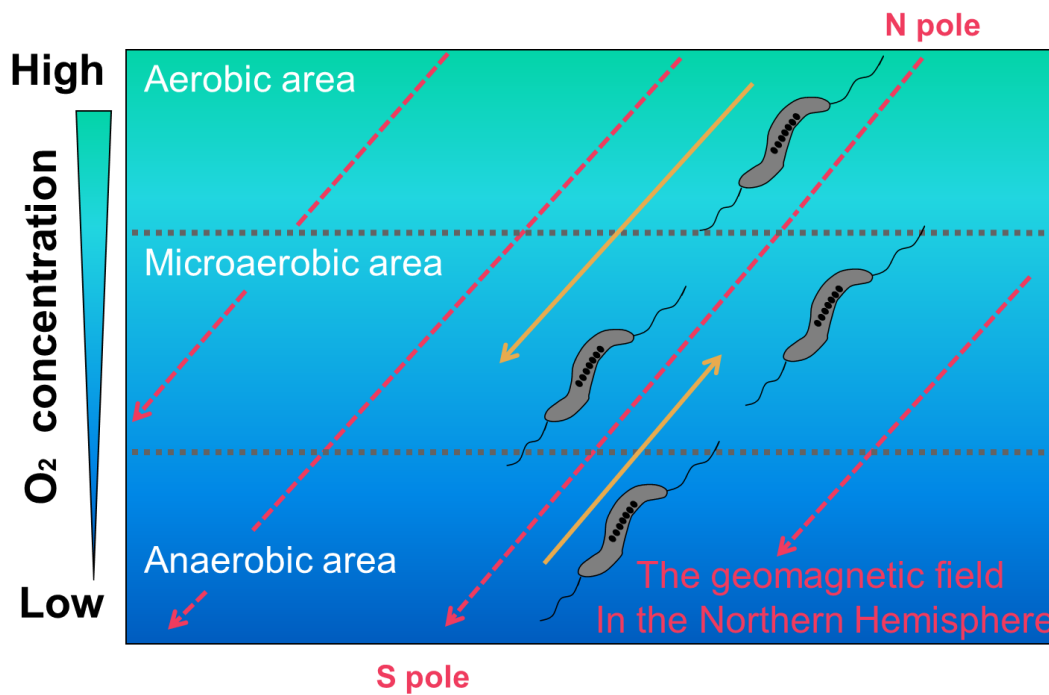*Magnetospirillum magneticum* AMB-1.

Fig. 1-2 Model of magneto-aerotaxis in the Northern Hemisphere. In the Northern Hemisphere, magnetotactic bacteria swim toward the magnetic S-pole. When magnetotactic bacteria reach the anaerobic area, they switch the swimming direction and swim toward the magnetic N pole. Consequently, magnetotactic bacteria can remain in their favorable microaerobic area.
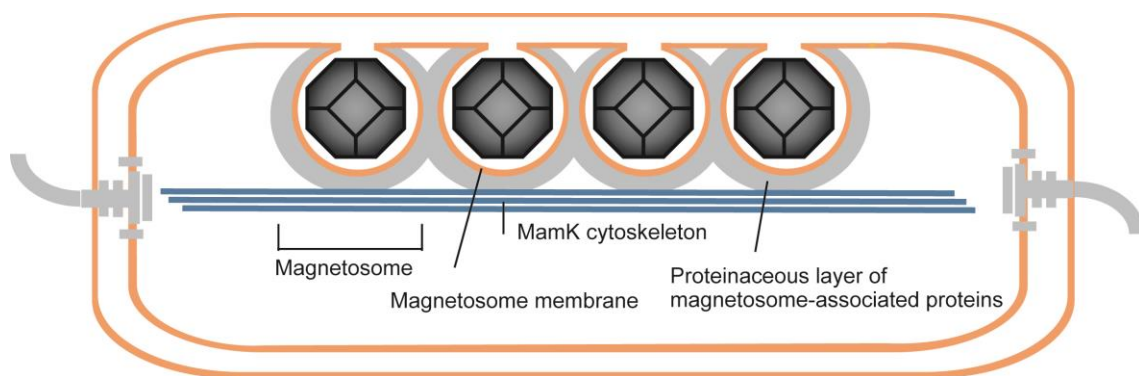
Fig. 1-3 Schematics of structure of magnetosome. Magnetosomes consist of regular-sized magnetite or greigite nanocrystals enveloped with phospholipid bilayer membrane and magnetosome-associated proteins. Magnetosomes are arranged in one or multiple chains along the cytoskeletal protein MamK. Magnetosome vesicles are continuous to cytoplasmic membrane via narrow constrictions.
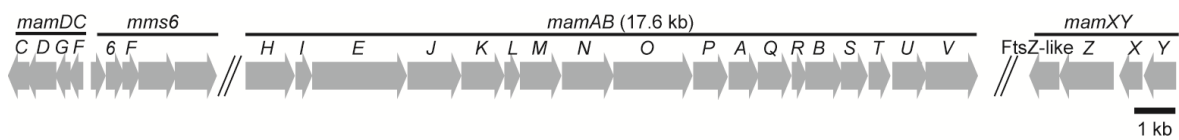
Fig. 1-4 Schematics of magnetosome island in *M. magneticum* AMB-1. Magnetosome island contains four core operons: *mamDC*, *mms6*, *mamAB* and *mamXY* operons.
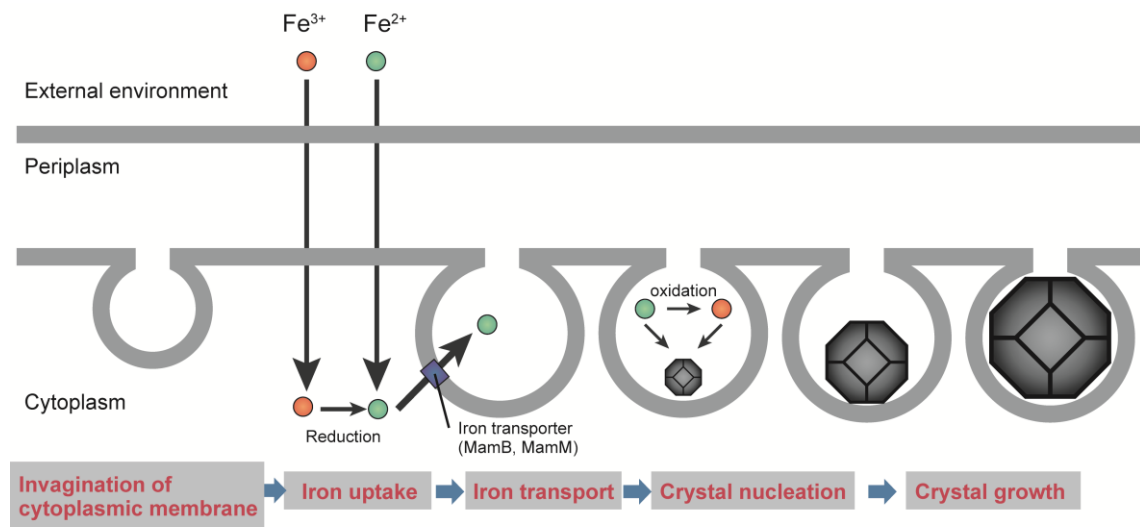
Fig. 1-5 Model of magnetosome formation and magnetite biomineralization. First,

magnetosome vesicles are formed throughout the cell by invagination of the cytoplasmic

membrane. Second, iron is transported from the cytoplasm into the magnetosome vesicle

by iron transporters localized in the magnetosome membrane. Third, a single magnetite

crystal is nucleated in the magnetosome lumen; then, a regular-shaped cuboctahedral

magnetite crystal is grown until it reaches approximately 50 nm in diameter.

Chapter II

Measuring intracellular pH using

pH-sensitive fluorescent proteins

Introduction

pH regulation in organelles provides an optimal environment for essential specific reactions of individual organelles, such as ATP generation in the mitochondria and proteolysis in the lysosome (Casey et al., 2010). Therefore, measuring the pH of intracellular compartments is necessary to understand the functions and states of the organelles. Recent advances in imaging techniques using GFP-derived, pH-sensitive fluorescent proteins, such as pHluorin (Miesenböck et al., 1998), DeGFP (Hanson et al., 2002), and E^2GFP (Bizzarri et al., 2006), make an avenue to measure the pH in microcompartments, such as the cytoplasm, peroxisome, endosome, trans-Golgi network, and presynaptic secretory vesicles, in living eukaryotic cells (Bizzarri et al., 2009). However, half a century ago, bacterial cells were thought of as simple "bags of enzymes," and compartmentalization was a hallmark of eukaryotic cells. Currently, it is known that bacterial cells produce nano-sized ordered membrane-bound compartments (Cornejo et al., 2014; Kerfeld et al., 2010; Munõz-Gómez et al., 2017), such as anammoxosomes (van Niftrik, 2013; Neumann et al., 2014) and magnetosomes (Blakemore, 1975), which are called prokaryotic organelles that are counterparts of corresponding eukaryotic organelles (Cornejo et al., 2014). However, the internal environment of the prokaryotic organelle in a living bacterial cell has not been investigated. Here, I investigated pH in cytoplasm, periplasm and magnetosomes of a living magnetotactic bacterium *Magnetospirillum magneticum* AMB-1 using the pH-sensitive fluorescent protein E^2GFP as a fusion protein (Fig. 2-1).

Materials and Methods

Microorganisms and cultures.

Composition of the medium for cultivation of *M. magneticum* AMB-1 is shown in Table 2-1. Bacterial strains and plasmids are summarized in Table 2-2. *M. magneticum* AMB-1 (ATCC 700264) was cultured as previously described (Mastunaga et al., 1991). *Escherichia coli* strains were cultivated in LB broth (Sambrook & Russel, 2001) at 37˚C, unless specified otherwise. When necessary, the antibiotic kanamycin was added at 5 µg/ml for AMB-1 and 20 µg/ml for *E. coli*. For cultivating *E. coli* WM3064, the medium was supplemented with 0.3 mM diaminopimelic acid.

Expression of pH-sensitive fluorescent protein E^{2}GFP in M. magneticum AMB-1.

Schematics of pH measurement using E^{2}GFP fusion proteins is shown in Fig. 2-1. Primer sequences used in this study are listed in Table 2-3.To express recombinant proteins in AMB-1 cells, the broad-host-range protein expression vector pBBR111 harboring tac promoter was used (Philippe & Wu, 2010). Artificially synthesized *E^{2}GFP* with codon optimization was purchased from Eurofins, Tokyo, Japan. DNA fragments of *E^{2}GFP* for cytoplasmic expression were obtained using PCR amplification with primers e2gfp_inf_F and e2gfp_inf_R and template pTAKN-2-E^{2}GFP. Linearized pBBR111 was obtained using PCR with primers pBBR111_F_infusion and pBBR111_R_infusion and template pBBR111. Linearized pBBR111 and *E^{2}GFP* DNA fragments were assembled into pBBR111-E^{2}GFP using the In-Fusion cloning system (TaKaRa Bio). For periplasmic expression of E^{2}GFP, the signal sequence of the twin-arginine translocation (Tat) pathway derived from the periplasmic nitrate reductase NapA was

inserted at the N-terminus of E^2GFP. DNA fragments coding for the signal sequence (1-34 amino acid residues of NapA) were amplified from AMB-1 genomic DNA using primers napA_inf_F and napA_inf_R. DNA fragments of E^2GFP was amplified using the primers napA-e2gfp_inf_F and e2gfp_inf_R and template pTAKN-2-E^2GFP. Linearized pBBR111 was obtained using PCR with primers pBBR111_F_infusion and pBBR111_R_infusion and template pBBR111. Linearized pBBR111 and DNA fragments of NapA$^{1-34}$ and E^2GFP were assembled into pBBR111-napA$^{1-34}$-E^2GFP using the In-Fusion cloning system (TaKaRa Bio). To express E^2GFP in magnetosomes, magnetosome-associated proteins MamC and Mms6 were used as fusion proteins. For the expression of MamC-E^2GFP, linearized vectors were prepared using PCR with primers pBBR111-mamC-gfp_inf_R and pBBR111_R_infusion and template pBBR111_mamC-gfp. DNA fragments of E^2GFP was amplified from pTAKN-2-E^2GFP using the primers c6-e2gfp_inf_F and e2gfp_inf_R. The linearized vector and E^2GFP were assembled into pBBR111-mamC-E^2GFP using the In-Fusion cloning system (TaKaRa Bio). For the expression of Mms6-E^2GFP, linearized vectors were prepared using PCR with primers pBBR111_F_infusion and pBBR111_R_infusion and template pBBR111. DNA fragments of *mms6* were amplified from genomic DNA of AMB-1 using the primers mms6-e2gfp_inf_F and mms6-e2gfp_inf_R. E^2GFP fragments were amplified using the primers c6-e2gfp_inf_F and e2gfp_inf_R and template pTAKN-2-E^2GFP. Linearized vector and fragments of *mms6* and E^2GFP were assembled into pBBR111-E^2GFP using the In-Fusion cloning system (TaKaRa Bio). These vectors were introduced into AMB-1 by conjugation with *E. coli* WM3064 as previously described (Komeili et al., 2004).

pH measurement using a fluorescence spectrophotometer.

For bulk measurement of intracellular pH, emission spectra were obtained using the fluorescence spectrophotometer Shimadzu RF-5300PC (Shimadzu, Japan). AMB-1 cells were collected by centrifugation at 5,600 x g for 10 min at room temperature, and the pellet containing cells was resuspended in distilled water. Aliquots of the cell suspension were centrifuged again, and supernatant was completely removed. For calibration, cells were resuspended in calibration buffers adjusted to various pH values using 0.1 M citrate and 0.2 M Na_2HPO_4 in varying ratios. To equilibrate the pH between the cytoplasm and buffers, 20 mM sodium benzoate was added to the buffer solutions (Wilks and Slonczewski 2007). The optical density of the cell suspension in each buffer at 600 nm was set at 0.2. The emission spectra of the cell suspensions in

$$R_a = \frac{F(\lambda x_{488\ nm}, \lambda e_{515-535\ nm})}{F(\lambda x_{458\ nm}, \lambda e_{495-515\ nm})}$$

$$R_a = R_0 \times \left(\frac{R_f + 10^{(pK'-pH)}}{1 + 10^{(pK'-pH)}} \right) \qquad (1)$$

calibration buffers excited at 488 and 458 nm were obtained at room temperature. The standard curve for bulk pH measurement was obtained using the following equation:

where R_a is the ratio of the addition of fluorescence intensities ranging between 515 and 535 nm excited at 488 nm to that of fluorescence intensities ranging between495 and 515 nm excited at 458 nm. Based on the least square method, the parameters R_0, R_f, and pK' were determined to be 0.630, 2.46, and 7.08, respectively. To measure the pH, collected cells producing E^2GFP or $NapA^{1-34}$-E^2GFP were resuspended in vitamin-free MS-1 liquid medium, and optical densities of the cell suspensions were adjusted to 0.2. Emission spectra of these cell suspensions were

obtained, and cytoplasmic and periplasmic pH were estimated based on equation (1) and the determined parameter values. For carbonyl cyanide m-chlorophenyl hydrazine (CCCP) treatment, 15 µl of 1 mM CCCP solution (final concentration, 5 µM) was added to 3 ml of the cell suspension, and emission spectrum was obtained after 5 min of CCCP addition.

Highly inclined and laminated optical sheet (HILO) microscopy.

Bacteria were imaged using a total internal reflection fluorescence (TIRF) microscopy-based system with an inverted microscope (Nikon Ti-E) equipped with a 100x CFI Apo TIRF objective lens (Nikon). A 488-nm laser (Sapphire; Coherent) was used to illuminate the sample at an inclined angle, which is slightly steeper than the critical angle required for total reflection in order to illuminate an entire bacterial cell. The angle of the laser beam was adjusted manually to optimize the signal-to-noise ratio.

pH measurements for single cells.

To measure pH in single cells, I used the HILO microscope (Nikon Ti-E) equipped with a grating spectrometer (CLP-50; Andor Technology). Schematic representation of the optical system is shown in Fig. 2-2. Samples were excited by oblique illumination using a 488-nm laser (Sapphire; Coherent). Fluorescence light was passed through a dichroic filter (Di02-R488-25x36; Semrock) and long-pass emission filter (BLP01-488R-25; Semrock). To obtain the emission spectra, grating and slit (0.1 mm) of the CLP-50 spectrometer were inserted, and spectral images were acquired using a highly sensitive electron-multiplying charge-coupled device camera (iXon3; Andor, DU897E-CS0) with EM and preamplifier gains of 296 and 2.4x, respectively. For *in vivo* calibration, 20 µl of E^2GFP-containing cell suspension along with the

calibration buffer described above were added onto poly-L-lysine-coated cover slips embedded with Attofluor cell chambers (Thermo Fisher Scientific). Emission spectra of single cells in calibration buffers excited at 488 nm were obtained, and a standard curve of pH vs. fluorescence ratio (R_b) was obtained using the following equation:

$$R_b = \frac{F(\lambda x_{488\,nm}, \lambda e_{522-524\,nm})}{F(\lambda x_{488\,nm}, \lambda e_{508-510\,nm})}$$

$$R_b = R_0 \times \left(\frac{R_f + 10^{(pK' - pH)}}{1 + 10^{(pK' - pH)}} \right) \qquad (2)$$

where R_b is the ratio of the addition of fluorescence intensities ranging between 522 and 524 nm to that of fluorescence intensities ranging between 508 and 510 nm, for single cells. The R_0, R_f, and pK' were determined to be 1.12, 3.89, and 7.05, respectively. For pH measurement, 20 µl of the cell suspension in vitamin-free MS-1 liquid medium was applied to cell chambers, and emission spectra of single cells were obtained. Cellular pH was estimated using equation (2) and the determined parameter values.

Preparation of subcellular fractions.

Membrane, soluble, and magnetosome fractions were prepared as previously described (Nguyen et al., 2016).

SDS-PAGE and immunochemical analysis.

SDS-PAGE was performed according to the method of Laemmli (Laemmli 1970). Immunoblotting analysis was performed as previously described (Taoka et al., 2014). The anti-

GFP polyclonal antibody (MBL) was diluted to 1:10,000. Goat anti-rabbit IgG conjugated with horseradish peroxidase (GE Healthcare) was diluted to 1:10,000 using the Pierce Western Blotting Substrate Plus. Chemiluminescence data were collected using a luminescent image analyzer (LAS 3000; Fujifilm).

Results

Measurement of cytoplasmic and periplasmic pH in M. magneticum AMB-1 cells using E^{2}GFP

The pH-sensitive fluorescent protein E^{2}GFP showed spectral forms that were convertible upon pH changes during both excitation and emission, with pK value close to 7.0 (Bizzarri et al., 2006). I measured pH in *M. magneticum* AMB-1 using E^{2}GFP. In this study, E^{2}GFP emission spectra at 488 and 458 nm obtained using a fluorescence spectrophotometer were used to estimate the pH of AMB-1 cells in liquid medium. E^{2}GFP or E^{2}GFP fusion proteins were expressed in AMB-1 cells from the broad-host-range plasmid pBBR111 (Philippe & Wu 2010). To measure the periplasmic pH of AMB-1, the N-terminal signal sequence of NapA (Taoka et al., 2003), which is the catalytic subunit of periplasmic nitrate reductase from AMB-1, was used for periplasmic targeting of E^{2}GFP. The N-terminal 34-amino acid sequence of NapA, NapA$^{1-34}$, contains the predicted signal sequence for the Tat pathway (Taoka et al., 2003), which reported a suitable pathway for GFP periplasmic translocation (Feilmeier et al., 2000). The expressions of E^{2}GFP and NapA$^{1-34}$-EGFP in AMB-1 cells were confirmed using immunoblotting of cell lysates with an anti-GFP antibody (Fig. 2-3). The cell lysate from NapA$^{1-34}$-E^{2}GFP-expressing cells showed two positive bands at 27 and 30 kDa, which corresponded to the predicted molecular masses of the signal peptide-digested matu^{2}re E^{2}GFP and precursor NapA$^{1-34}$-E^{2}GFP, respectively. The abundance of the 27-kDa positive band indicated that most E^{2}GFP was translocated to the periplasm in NapA$^{1-34}$-E^{2}GFP-expressing cells (Fig. 2-3). Hereafter, un-tagged E^{2}GFP- and NapA$^{1-34}$-E^{2}GFP-expressing cells are referred to as cytosolic and periplasmic E^{2}GFP-expressing cells, respectively.

To use the E^2GFP signals as a measure of cellular pH, a standard curve for the pH-dependent R_a was generated (Fig. 2-4). The pH-dependent fluorescence emission spectra were obtained from E^2GFP-expressing cell suspensions in citrate/phosphate buffers, which were produced over a range of pH values in the presence of the permeating acid sodium benzoate to equilibrate the pH between the cytoplasm and buffers (Wilks & Slonczewski 2007). Figures 2-4 A and B shows the spectra obtained from cell suspensions at pH ranging from 4.7 to 9.2. The fit curve showed a linear correlation between pH ranging from ~6–~8 (Fig. 2-4 C). Note that the pH range was suitable to evaluate physiological pH.

I measured the cytosplasmic and periplasmic pH of cells from early stationary phase cultures. Before measurement, the cells were suspended in a vitamin-free fresh liquid medium to remove the fluorescence noise due to vitamin components. Figure 2-5 shows the emission spectra of cytosolic and periplasmic E^2GFP-expressing cells. The peak of the emission spectrum at 524 nm excited at 488 nm in the cytosolic E^2GFP-expressing cells had higher intensity than that in the periplasmic E^2GFP-expressing cells (Fig. 2-5 A). On the other hand, the peak of the periplasmic E^2GFP-expressing cells excited at 458 nm was blue-shifted compared with the cytosolic E^2GFP-expressing cells (Fig. 2-5 B). Based on the standard curve shown in Fig. 2-4 C, the average pH values of the cytoplasm and periplasm in AMB-1 cells were estimated to be 7.6 and 6.8, respectively. Next, I measured the pH of cells treated with the protonophore CCCP (Fig.2-6). The 5-μM CCCP treatment affected the spectra of the cytosolic E^2GFP-expressing cells (Fig. 2-6 A and B). The estimated cytoplasmic pH dropped from 7.6 to 6.9 due to the CCCP treatment, whereas the estimated periplasmic pH did not change (Fig. 2-6 C and D), indicating that protons flowed into the cytoplasm from the periplasm or extracellular milieu due to the

protonophore treatment. This result demonstrated that the pH measurement method using E²GFP emission was functional in AMB-1 cells.

Single cell pH measurement using microspectroscopy.

As described above, I estimated the intracellular pH of AMB-1 cell suspension using a fluorospectrophotometer. Because the obtained fluorescence signals were the summation of the fluorescence from cells in the suspension, the pH of a single cell or cellular component in a single cell could not be estimated using this method. Hence, I measured the pH of a single living cell using highly inclined and laminated optical sheet (HILO) microscopy equipped with a grating spectrometer (Fig. 2-2). HILO microscopy provides a high signal-to-noise ratio for the fluorescence image of a bacterial cell (Yao and Carballido 2014). Previously, Taoka et al. succeeded in imaging the dynamic movement of magnetosomes in a living AMB-1 cell using HILO microscopy (Taoka et al., 2017). The E²GFP fluorescence signal was obtained from a cell attached to a poly-L-lysine-coated cover slip. To obtain the standard curve for the estimation of pH, emission spectra at 488 nm of cytosolic E²GFP-expressing cells were obtained in the citrate/phosphate buffers (pH = 5.1–9.0) (Fig. 2-7 A). R_b at each pH was quantified using emission spectra obtained from 10 cells. R_b values showed a ratiometric curve fitted by equation (2) (Fig. 2-7 B). The cytoplasmic and periplasmic pH values were estimated using the cytoplasmic and periplasmic E²GFP-expressing cells (n = 65 and 74, respectively) that were harvested from the stationary growth phase cultures. Figure 2-8 shows the distributions of cytoplasmic and periplasmic pH values estimated from individual cells. The cytoplasmic and periplasmic medians of pH values were 7.6 and 7.2, respectively (Fig. 2-8, and Table 2-4), and the cytoplasmic and periplasmic pH distributions were significantly different (Mann–Whitney

U test; p < 0.001). The cytoplasmic pH values were >7, whereas the periplasmic pH was widely distributed between 6.3 and 8.2 (Fig. 2-8 A). The pH distributions obtained from single cell measurements corresponded with pH values obtained from the cell suspension using the fluorospectrophotometer (Fig. 2-5).

pH estimation in the magnetosome.

Next, I estimated pH values inside and outside (cytoplasmic surface) the magnetosome vesicle. For this, C-terminal E^2GFP-fused magnetosome-associated membrane proteins Mms6-E^2GFP and MamC-E^2GFP were used for targeting E^2GFP to the inside and outside of the magnetosome vesicle, respectively (Fig. 2-1 and Fig. 2-9). Both Mms6 and MamC (also called Mms13) are magnetosome-associated transmembrane proteins involved in controlling magnetite crystal shape in the magnetosome vesicle. Mms6 has a single transmembrane helix, and is involved in the biomineralization of cubo-octahedral magnetite crystals both *in vitro* (Arakaki et al., 2003; Amemiya et al., 2007) and *in vivo* (Tanaka et al., 2011; Yamagishi et al., 2016). It has been demonstrated that the C-terminal region of Mms6 strongly binds magnetite crystal in the magnetosome vesicle (Arakaki et al., 2003; Amemiya et al., 2007). On the other hand, MamC has two transmembrane helices, and the loop region between the helices contains an iron-binding site (Nudelman et al., 2016). Moreover, a protease protection assay using luciferase fused to the C-terminus of MamC indicated that it localizes on the cytoplasmic surface of magnetosomes in *M. magneticum* AMB-1 (Yoshino & Matsunaga 2006). Therefore, the E^2GFP-fused C-terminal regions of Mms6 and MamC should be localized inside the magnetosome vesicle and on the cytoplasmic surface of the magnetosome vesicle, respectively (Fig. 2-1 and Fig. 2-9).

Subcellular localization of MamC-E^{2}GFP and Mms6-E^{2}GFP was confirmed using immunoblotting (Fig. 2-10). Both MamC-E^{2}GFP and Mms6-E^{2}GFP specifically localized in the magnetosome fraction. According to fluorescence microscopic images of Mms6-E^{2}GFP and MamC-E^{2}GFP-expressing cells, GFP fluorescence along the long axis of the cells indicated magnetosome localization of E^{2}GFP (Fig. 2-11). I also estimated the pH values inside and outside the magnetosome using HILO microscopy equipped with a grating spectrometer. Figure 2-12 shows the pH distributions of Mms6-E^{2}GFP and MamC-E^{2}GFP-expressing cells in the stationary and exponential growth phases. Interestingly, the pH values estimated using Mms6-E^{2}GFP (inside vesicle) were specifically altered during the growth phase. The median pH inside the vesicle was 7.4 and 7.0 in the exponential and stationary growth phases, respectively (Mann–Whitney U test; $p < 0.001$), whereas that outside the vesicle did not significantly differ between the growth phases (Mann–Whitney U test; $p = 0.7$) (Fig. 2-12, and Table 2-4). These results demonstrated that magnetosome vesicles were specifically alkalinized in the exponential growth phase.

Discussion

Bacterial cells maintain their cellular pH because most proteins require distinct pH ranges in order to function (Krulwich et al., 2011). Here, I developed a pH measurement method for the cytoplasm, periplasm, and magnetosomes in a single living cell of the magnetotactic bacterium *M. magneticum* AMB-1 using E^2GFP. The cytoplasmic and periplasmic pH values of AMB-1 cells estimated in this study were fitted to those previously obtained from the neutralophilic bacteria *E. coli* (Zilberstein et al., 1979) and *Bacillus subtilis* (Shioi et al., 1978). I assessed pH values in the magnetosome lumen and on the cytoplasmic surface of magnetosomes using Mms6-E^2GFP and MamC-E^2GFP, respectively. This is the first report regarding pH measurement in the magnetosome. Interestingly, the pH in the magnetosome lumen increased during the exponential growth phase, whereas that on the cytoplasmic surface did not change between the exponential and stationary growth phases (Fig. 2-12). Generally, the number of crystals in cells are reduced and the magnetism of cells is decreased during the exponential growth phase because of cell division, but they recover during the late exponential/early stationary phase; thus, crystal synthesis occurs in cells during this stage. The increasing pH in the exponential phase may be related to magnetosome synthesis.

MamB and MamM, two abundant magnetosome-associated proteins (Grünberg et al., 2004), are multifunctional and involved in several steps of magnetosome formation, including magnetosome vesicle formation and transportation of ions for magnetite nucleation (Uebe et al., 2011; Uebe et al 2017; Zeytuni et al., 2014). Both MamB and MamM are homologs of the cation diffusion facilitator (CDF) family. Because the members of the CDF family transport divalent transition metal cations, including Zn^{2+}, Co^{2+}, Cd^{2+}, Mn^{2+}, Ni^{2+}, and Fe^{2+}, from the cytoplasm

into the intracellular compartments or periplasmic or extracellular space using the proton motive force (Nies, 2003; Grass et al., 2005; Rosch et al., 2009), MamB and MamM were implicated in magnetosomal ferrous ion/proton antiporters to accumulate iron in the magnetosome vesicle for magnetite synthesis from the cytoplasm into the magnetosome lumen. Thus, increased pH in the magnetosome lumen may be due to proton consumption in iron uptake into the magnetosome lumen.

The periplasmic pH of AMB-1 cells showed a wider distribution than that of the cytoplasm, and the periplasmic pH of a portion of cells overlapped with the cytoplasmic pH (Fig. 2-8). This might be due to the transportation efficiency of periplasmic E^2GFP in individual cells. At the single-cell level, the transportation efficiency may not be homogenous between the cells. The periplasmic pH seems to be overestimated in the cells containing a high percentage of the precursor NapA$^{1-34}$-E^{2}GFP in the cytosplasm.

It is generally known that pH homeostasis in organelles is spatio-temporally regulated to accomplish the specialized roles of individual organelles. As stated above, the magnetosome organelle has a distinct function in mineralizing the magnetite crystal; thus, pH homeostasis in the magnetosome lumen should be controlled to accomplish its specific roles similar to eukaryotic organelles. For instance, the optimal proton concentration in the magnetosome lumen should be maintained during magnetite synthesis to supply iron ions for magnetite mineralizing. The protons, which are consumed in iron transport using the ferrous ion/proton antiporters, should be replenished into the magnetosome lumen until when the magnetosome lumen is occupied by a mature magnetite crystal. However, the mechanism for maintenance of pH homeostasis in the magnetosome is not studied, yet.

As the next step, further improvements in my live-cell pH measurement method will help to elucidate pH changes in the magnetosome lumen during mineralization in high spatiotemporal resolution. Understanding of the mechanism for magnetosome pH homeostasis provides a clue to reveal molecular mechanisms of magnetite biomineralization in the bacterial organelle.

References

Amemiya Y, Arakaki A, Staniland SS, Tanaka T, Matsunaga T. (2007) Controlled formation of magnetite crystal by partial oxidation of ferrous hydroxide in the presence of recombinant magnetotactic bacterial protein Mms6. *Biomaterials*. 28:5381-5389.

Arakaki A, Webb J, Matsunaga T. (2003) A novel protein tightly bound to bacterial magnetic particles in *Magnetospirillum magneticum* strain AMB-1. *J Biol Chem*. 278:8745-8750.

Bizzarri R, Arcangeli C, Arosio D, Ricci F, Faraci P, Cardarelli F, Beltram F. (2006) Development of a novel GFP-based ratiometric excitation and emission pH indicator for intracellular studies. *Biophys J*. 90:3300-3314.

Bizzarri R, Serresi M, Luin S, Beltram F. (2009) Green fluorescent protein based pH indicators for *in vivo* use: a review. *Anal Bioanal Chem*. 393:1107-1122.

Blakemore R. (1975) Magnetotactic bacteria. *Science*. 190:377-379.

Casey JR, Grinstein S, Orlowski J. (2010) Sensors and regulators of intracellular pH. *Nat Rev Mol Cell Biol*. 11:50-61.

Cornejo E, Abreu N, Komeili A. (2014) Compartmentalization and organelle formation in bacteria. *Curr Opin Cell Biol*. 26:132-138.

Demarre G, Guérout AM, Matsumoto-Mashimo C, Rowe-Magnus DA, Marlière P, Mazel D. (2005). A new family of mobilizable suicide plasmids based on broad host range R388 plasmid (IncW) and RP4 plasmid (IncPalpha) conjugative machineries and their cognate *Escherichia*

coli host strains. *Res. Microbiol*. 156:245-255.

Feilmeier BJ, Iseminger G, Schroeder D, Webber H, Phillips GJ. (2000) Green fluorescent protein functions as a reporter for protein localization in *Escherichia coli*. *J Bacteriol*. 182:4068-4076.

Grass G, Otto M, Fricke B, Haney CJ, Rensing C, Nies DH, Munkelt D. (2005) FieF (YiiP) from *Escherichia coli* mediates decreased cellular accumulation of iron and relieves iron stress. *Arch Microbiol*. 183:9-18.

Grünberg K, Muller EC, Otto A, Reszka R, Linder D, Kube M, Reinhardt R, Schüler D. (2004) Biochemical and proteomic analysis of the magnetosome membrane in *Magnetospirillum gryphiswaldense*. *Appl Environ Microbiol*. 70:1040-1050.

Hanson GT, McAnaney TB, Park ES, Rendell ME, Yarbrough DK, Chu S, Xi L, Boxer SG, Montrose MH, Remington SJ. (2002) Green fluorescent protein variants as ratiometric dual emission pH sensors. 1. Structural characterization and preliminary application. *Biochemistry*. 41:15477-15488.

Kerfeld CA, Heinhorst S, Cannon GC. (2010) Bacterial microcompartments. *Annu Rev Microbiol*. 64:391-408.

Komeili A, Vali H, Beveridge TJ, Newman DK. (2004) Magnetosome vesicles are present before magnetite formation, and MamA is required for their activation. *Proc Natl Acad Sci U S A*. 101:3839-3844.

Krulwich TA, Sachs G, Padan E. (2011) Molecular aspects of bacterial pH sensing and

homeostasis. *Nat Rev Microbiol*. 9:330-343.

Laemmli UK. (1970) Cleavage of structural proteins during the assembly of the head of bacteriophage T4. *Nature*. 227:680-685.

Matsunaga T, Sakaguchi, T., Tadakoro, F. (1991) Magnetite formation by a magnetic bacterium capable of growing aerobically. *Appl Microbiol Biotech*. 35:651-655.

Miesenböck G, De Angelis DA, Rothman JE. (1998) Visualizing secretion and synaptic transmission with pH-sensitive green fluorescent proteins. *Nature*. 394:192-195.

Munõz-Gómez SA, Wideman JG, Roger AJ, Slamovits CH. (2017) The origin of mitochondrial cristae from *Alphaproteobacteria*. *Mol Biol Evol*. 34:943-956.

Neumann S, Wessels HJ, Rijpstra WI, Sinninghe Damsté JS, Kartal B, Jetten MS, van Niftrik L. (2014) Isolation and characterization of a prokaryotic cell organelle from the anammox bacterium *Kuenenia stuttgartiensis*. *Mol Microbiol.* 94:794-802.

Nguyen HV, Suzuki E, Oestreicher Z, Minamide H, Endoh H, Fukumori Y, Taoka A. (2016) A protein-protein interaction in magnetosomes: TPR protein MamA interacts with an Mms6 protein. *Biochem Biophys Rep*. 7:39-44.

Nies DH. (2003) Efflux-mediated heavy metal resistance in prokaryotes. *FEMS Microbiol Rev*. 27:313-339.

Nudelman H, Valverde-Tercedor C, Kolusheva S, Perez Gonzalez T, Widdrat M, Grimberg N, Levi H, Nelkenbaum O, Davidov G, Faivre D, Jimenez-Lopez C, Zarivach R. (2016) Structure-

function studies of the magnetite-biomineralizing magnetosome-associated protein MamC. *J Struct Biol*. 194:244-252.

Philippe N, Wu LF. (2010) An MCP-like protein interacts with the MamK cytoskeleton and is involved in magnetotaxis in *Magnetospirillum magneticum* AMB-1. *J Mol Biol*. 400:309-322.

Rosch JW, Gao G, Ridout G, Wang YD, Tuomanen EI. (2009) Role of the manganese efflux system *mntE* for signalling and pathogenesis in *Streptococcus pneumoniae*. *Mol Microbiol*. 72:12-25.

Sambrook JR, Russel DW. (2001). Molecular cloning: a laboratory manual, 3rd ed. Cold Spring Harbor Laboratory Press, New York, NY.

Shioi JI, Imae Y, Oosawa F. (1978) Protonmotive force and motility of *Bacillus subtilis*. *J Bacteriol*. 133:1083-1088.

Tanaka M, Mazuyama E, Arakaki A, Matsunaga T. (2011) MMS6 protein regulates crystal morphology during nano-sized magnetite biomineralization *in vivo*. *J Biol Chem*. 286:6386-6392.

Taoka A, Eguchi Y, Mise S, Oestreicher Z, Uno F, Fukumori Y. (2014) A magnetosome-associated cytochrome MamP is critical for magnetite crystal growth during the exponential growth phase. *FEMS Microbiol Lett*. 358:21-29.

Taoka A, Kiyokawa A, Uesugi C, Kikuchi Y, Oestreicher Z, Morii K, Eguchi Y, Fukumori Y. (2017) Tethered magnets are the key to magnetotaxis: direct observations of *Magnetospirillum magneticum* AMB-1 show that MamK distributes magnetosome organelles equally to daughter

cells. *mBio*. 8: e00679-17.

Taoka A, Yoshimatsu K, Kanemori M, Fukumori Y. (2003) Nitrate reductase from the magnetotactic bacterium *Magnetospirillum magnetotacticum* MS-1: purification and sequence analyses. *Can J Microbiol*. 49:197-206.

Uebe R, Junge K, Henn V, Poxleitner G, Katzmann E, Plitzko JM, Zarivach R, Kasama T, Wanner G, Pósfai M, Böttger L, Matzanke B, Schüler D. (2011) The cation diffusion facilitator proteins MamB and MamM of *Magnetospirillum gryphiswaldense* have distinct and complex functions, and are involved in magnetite biomineralization and magnetosome membrane assembly. *Mol Microbiol*. 82:818-835.

Uebe R, Keren-Khadmy N, Zeytuni N, Katzmann E, Navon Y, Davidov G, Bitton R, Plitzko JM, Schüler D, Zarivach R. (2018) The dual role of MamB in magnetosome membrane assembly and magnetite biomineralization. *Mol Microbiol*. 107:542-557.

Uebe R, Schüler D. (2016) Magnetosome biogenesis in magnetotactic bacteria. *Nat Rev Microbiol*. 14:621-637.

Wilks JC, Slonczewski JL. (2007) pH of the cytoplasm and periplasm of *Escherichia coli*: rapid measurement by green fluorescent protein fluorimetry. *J Bacteriol*. 189:5601-5607.

Yamagishi A, Narumiya K, Tanaka M, Matsunaga T, Arakaki A. (2016) Core amino acid residues in the morphology-regulating protein, Mms6, for intracellular magnetite biomineralization. *Sci Rep*. 6:35670.

Yao Z, Carballido-López R. (2014) Fluorescence imaging for bacterial cell biology: from

localization to dynamics, from ensembles to single molecules. *Annu Rev Microbiol*. 68:459-476.

Yoshino T, Matsunaga T. Efficient and stable display of functional proteins on bacterial magnetic particles using Mms13 as a novel anchor molecule. (2006) *Appl Environ Microbiol*. 72:465-471.

Zeytuni N, Uebe R, Maes M, Davidov G, Baram M, Raschdorf O, Nadav-Tsubery M, Kolusheva S, Bitton R, Goobes G, Friedler A, Miller Y, Schüler D, Zarivach R. (2014) Cation diffusion facilitators transport initiation and regulation is mediated by cation induced conformational changes of the cytoplasmic domain. *PLoS One*. 9:e92141.

Zilberstein D, Schuldiner S, Padan E. (1979) Proton electrochemical gradient in *Escherichia coli* cells and its relation to active transport of lactose. *Biochemistry*. 18:669-673.

van Niftrik L. (2013) Cell biology of unique anammox bacteria that contain an energy conserving prokaryotic organelle. *Antonie van Leeuwenhoek*. 104:489-497.

Tables

Table 2-1 Composition of chemically defind medium (MSGM) for cultivation of *Magnetospirillum magneticum* AMB-1

MSGM

Distilled water	1 L
Wolfe's Vitamin Solution (see below)	10.0 ml
Wolfe's Mineral Solution (see below)	5.0 ml
Ferric Quinate Solution (see below)	2.0 ml
0.135% Resazurin	0.34 ml
KH_2PO_4	0.68 g
$NaNO_3$	0.12 g
Ascorbic acid	0.035 g
Tartaric acid	0.37 g
Succinic acid	0.37 g
Sodium acetate	0.082 g

The pH of the medium was adjusted to be 6.75 with NaOH.

Ferric Quinate solution:

$FeCl_3$	0.27 g
Quinic acid	0.19 g
Distilled water	100 ml

Wolfe's Vitamin Solution

Biotin	2.0 mg
Folic acid	2.0 mg
Pyridoxine HCl	10.0 g
Thiamine HCl	5.0 mg
Riboflavin	5.0 mg
Calcium D-(+)-pantothenate	5.0 mg
Nicotinic acid	5.0 mg
Cyanocobalamin	0.1 mg
p-Aminobenzoic acid	5.0 mg
Thioctic acid	5.0 mg
Distilled water	1 L

Wolfe's Mineral solution

Nitrilotriacetic acid	1.5g
$MgSO_4 \ 7H_2O$	3.0g
$MnSO_4 \ H_2O$	0.5g
NaCl	1.0g
$FeSO_4 \ 7H_2O$	0.1g
$CoCl_2 \ 6H_2O$	0.1g
$CaCl_2$	0.1g
$ZnSO_4 \ 7H_2O$	0.1g
$CuSO_4 \ 5H_2O$	0.01g
$AlK(SO_4)_2 \ 12H_2O$	0.01g
H_3BO_3	0.01g
$Na_2MoO_4 \ 2H_2O$	0.01g
Na_2SiO_3	4.88mg
Distilled water	1L

Add nitrilotriacetic acid was dissolved in approximately 500 ml of water and pH was adjusted to be about 6.5 with KOH to dissolve the compound.

Table 2-2. Bacterial stains and plasmid used in this study

Strains or plasmids	Relevant characteristic(s)	Reference or source
Escherichia coli		
XL-1 blue MRF'	Δ(*mcr*A)183 Δ(*mcr*CB-*hsd*SMR-*mrr*)173 *end*A1 *sup*E44 *thi*-1 *rec*A1 *gry*A96 *rel*A1 *lac* [F',*pro*AB,laqI^qZ ΔM15, Tn10(Tet^R)]	Stratagene
WM3064	*thrB1*004 *pro thi rpsL hsdS lacZ*Δ*M15* RP4-1360 Δ(*araBAD)567*Δ*dapA*1341::[*erm pir*]	Demarre et al. (2005)
Plasmids		
pTAKN-2- E²GFP		Eurofins
pBBR111	Protein expression vector for *M. magneticum* AMB-1; Tac promoter, *lacI^q*, Mob, Kan^r	Philippe & Wu (2010)
pBBR111_mamC-gfp	pBBR111 carrying *mamC-GFP*	Taoka et al. (2017)
pBBR111-E²GFP	pBBR111 carrying *E²GFP*	This study
pBBR111-napA-E²GFP	pBBR111 carrying *napA* (1-102)-*E²GFP*	This study
pBBR111-mamC-E²GFP	pBBR111 carrying *mamC-E²GFP*	This study
pBBR111-mms6-E²GFP	pBBR111 carrying *mms6-E²GFP*	This study

Table 2-3. Primers used in this study

Primer name	Sequences (5´-3´)
pBBR111_F_infusion	5´- CTCGAGTCCTCCTGTTTCCTGTG-3´
pBBR111_R_infusion	5´- GAATTCCTGCAGCCCGGGGGATCCAC-3´
e2gfp_inf_F	5´- ACAGGAGGACTCGAGATGAGCAAGGGCGAAGAG-3´
e2gfp_inf_R	5´- GGGCTGCAGGAATTCTCACTTGTAGAGCTCGTCCATGC-3´
napA_inf_F	5´- ACAGGAGGACTCGAGATGAGCCTCACCAGGCGC-3´
napA_inf_R	5´- GGCTTTTGCCGGCTGGGCGATGGCCGGCGT-3´
napA-e2gfp_inf_F	5´- CAGCCGGCAAAAGCCAGCAAGGGCGAAGAGCTG-3´
pBBR111-mamC-gfp_inf_R	5´- GAATTCCTGCAGCCCGGGGGATCCAC-3´
C6-e2gfp_inf_F	5´- GTGCCACGCGGTTCCATGAGCAAGGGCGAAGAG-3´
mms6-e2gfp_inf_F	5´- ACAGGAGGACTCGAGATGGGCGAGATGGAGCGC-3´
mms6-e2gfp_inf_R	5´- GGAACCGCGTGGCACCAGGGCCAGCGCGTCGCGCAG-3´

Table 2-4. pH values estimated using the single cell pH measurement by microspectroscopy

Characteristic of E^{2}GFP	Locus (growth phase)	Median pH	Number of cells
E^{2}GFP	Cytoplasm	7.6	65
NapA$^{1-34}$-E^{2}GFP	Periplasm	7.2	74
MamC-E^{2}GFP	Cytoplasmic surface of magnetosome (exponential phase)	7.2	84
MamC-E^{2}GFP	Cytoplasmic surface of magnetosome (stationary phase)	7.3	90
Mms6-E^{2}GFP	Magnetosome lumen (exponential phase)	7.4	91
Mms6-E^{2}GFP	Magnetosome lumen (stationary phase)	7.0	66

Figures
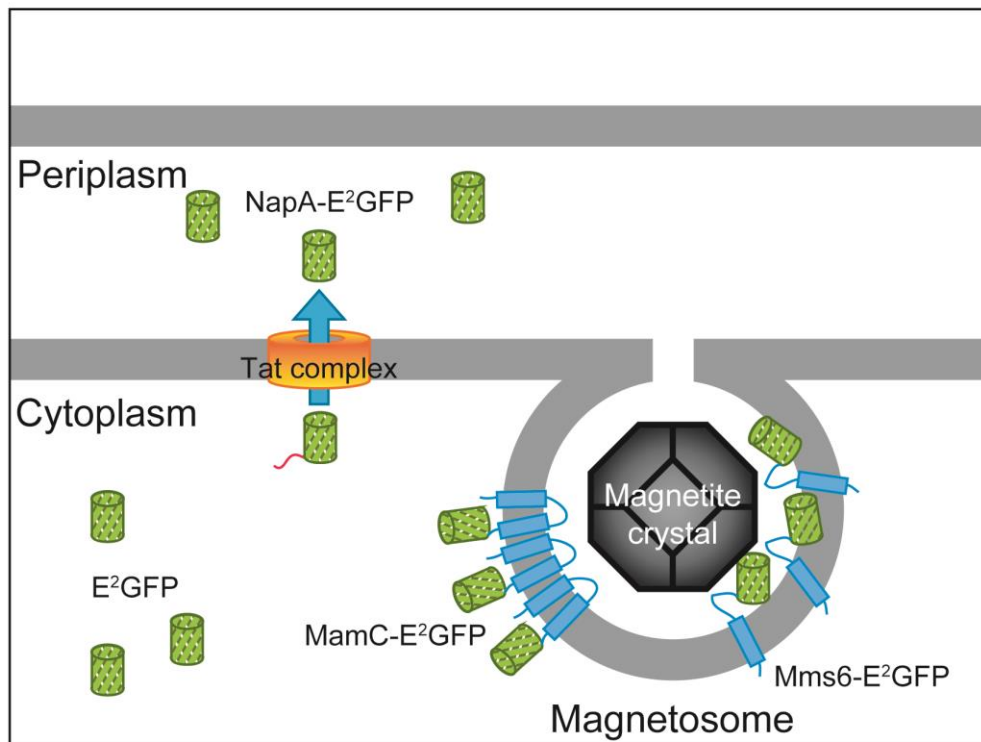
Fig. 2-1 Schematics of intracellular pH measurements using E^2GFP fusion proteins.
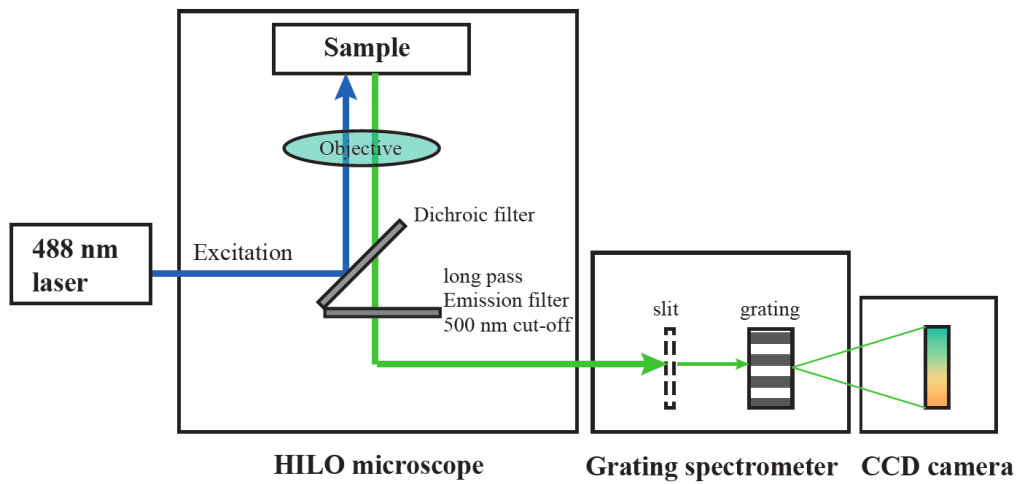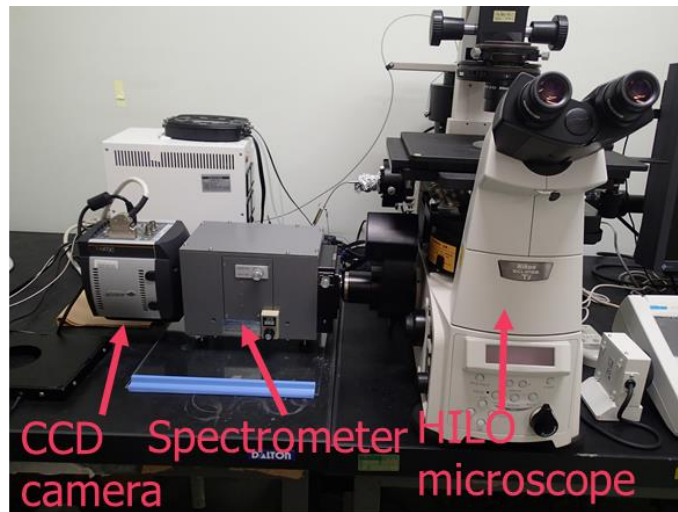
Fig. 2-2 Schematics of the laminated optical sheet (HILO) microscopy equipped with a grating spectrometer used in this study.
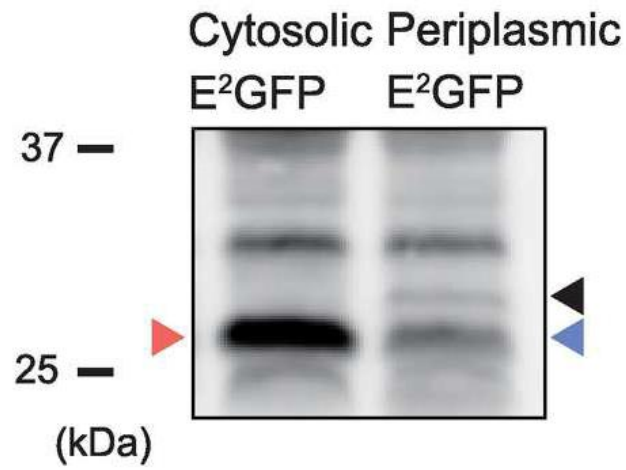
Fig. 2-3 Immunoblot of cytosolic E^2GFP and periplasmic E^2GFP in *M. magneticum AMB-1* cell extracts with anti-GFP antibodies. Pink, black, and blue triangles represent bands of cytosolic E^2GFP, full-length $NapA^{1-34}$-E^2GFP, and signal peptide-digested mature E^2GFP, respectively.
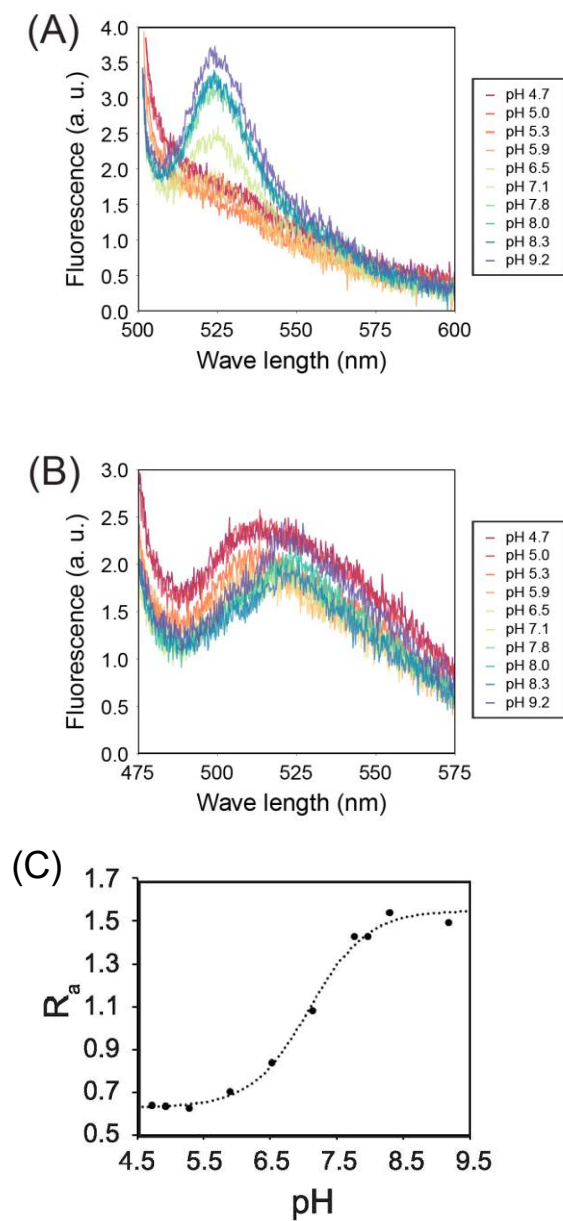
Fig. 2-4 Emission spectra obtained from cell suspensions at pH ranging from 4.7 to 9.2 at 488 nm (A) and 458 nm (B). (C) Standard curve of pH vs. fluorescence ratio obtained from emission spectra. Black circles and a dashed line indicates experimental values and a standard curve fitted to the equation (1) (see materials and methods section), respectively.
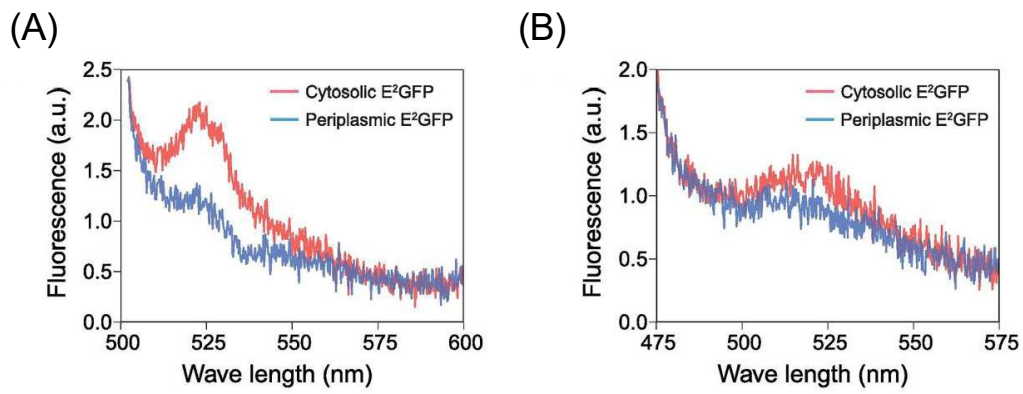
Fig. 2-5 Emission spectra of cytosolic (pink lines) and periplasmic (blue lines) E^2GFP-expressing cell suspensions excited at 488 nm (A) and 458 nm (B).
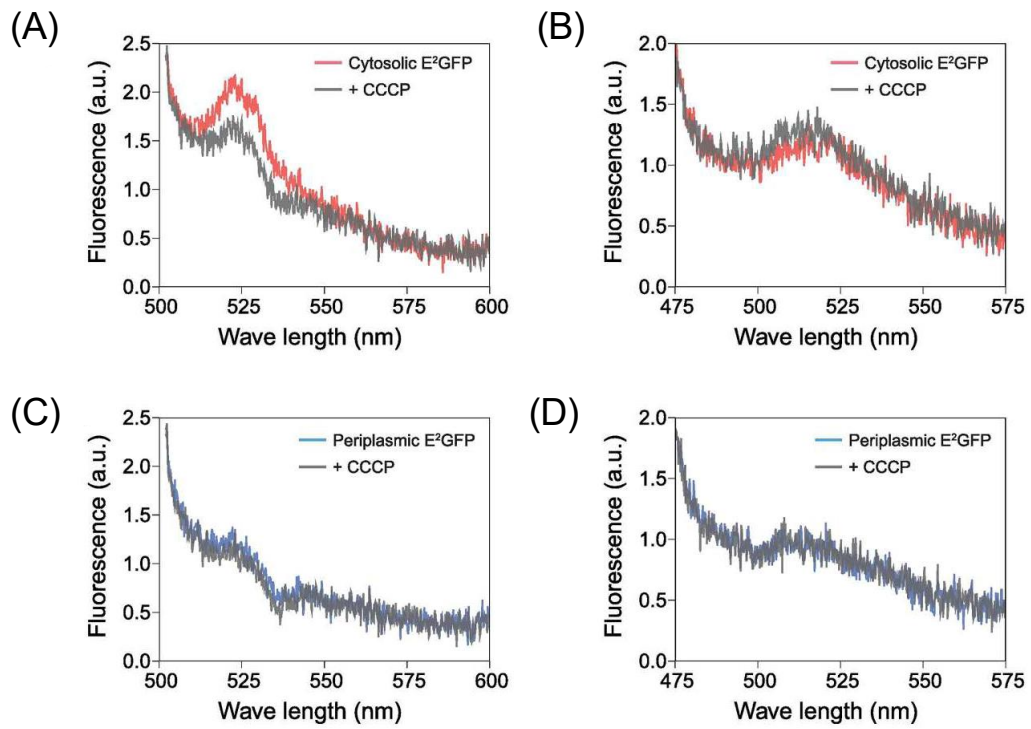
Fig. 2-6 Emission spectra of cytosolic (A, and B) and periplasmic (C, and D) E^2GFP-expressing cell suspensions excited at 488 nm (A, and C) and 458 nm (B, and D). Gray lines showed the emission spectra in the presence of CCCP.
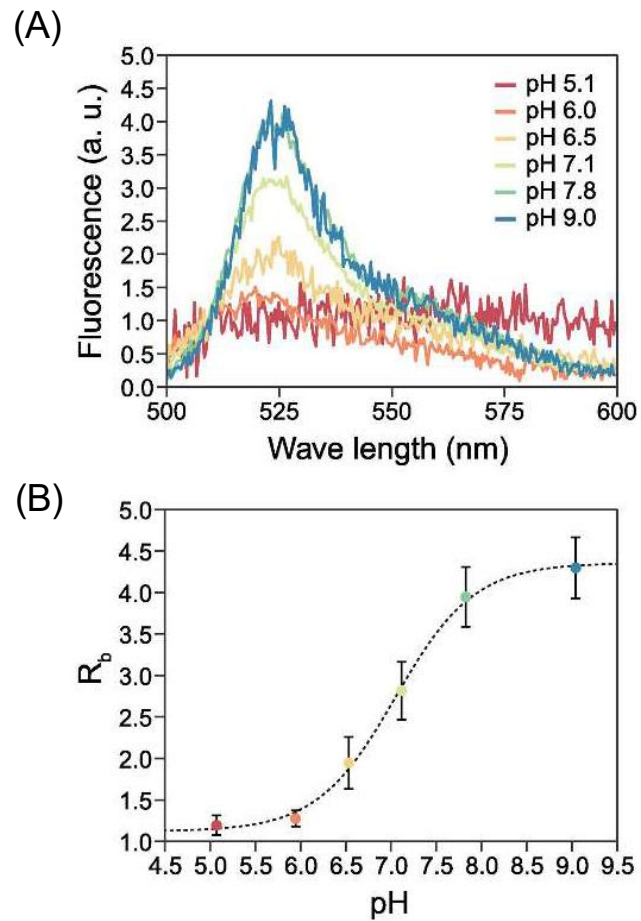
Fig. 2-7 (A) Representative emission spectra of E^2GFP-expressing cells in different pH buffers. Fluorescence intensities are represented as relative values with the intensities at 509 nm set as 1. (B) Standard curve of pH vs. fluorescence ratio obtained from emission spectra. The bars show standard deviations of R_b from emission spectra of individual cells (n = 10). The colors indicated pH values showed in panel (A).

(A)

(B)
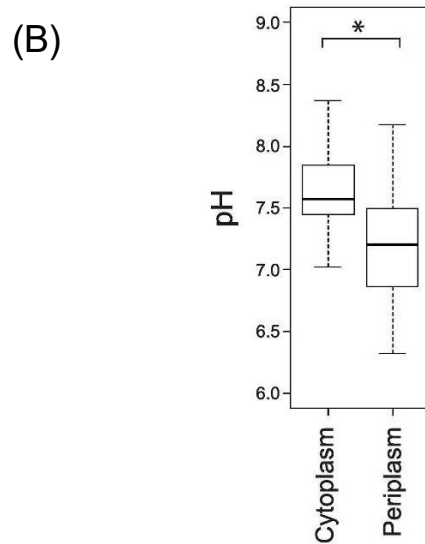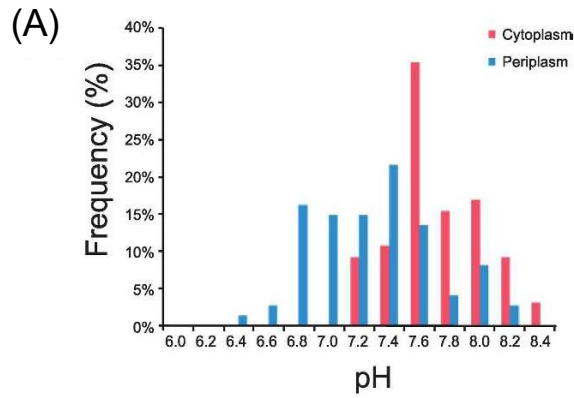
Fig. 2-8 Distributions of cytosolic and periplasmic pH. (A) Histogram of cytoplasmic (pink bars) and periplasmic (blue bars) pH. (B) Box plots of pH in the cytoplasm and periplasm. Solid lines in boxes indicate the median pH values. The asterisk represents statistical significance in the Mann–Whitney U test ($p < 0.001$).

Fig. 2-9 Schematics of E^{2}GFP fusion proteins used for measuring magnetosomal pH.

	Soluble fraction	Membrane fraction	Magnetosome fraction
MamC-E^{2}GFP			
Mms6-E^{2}GFP			
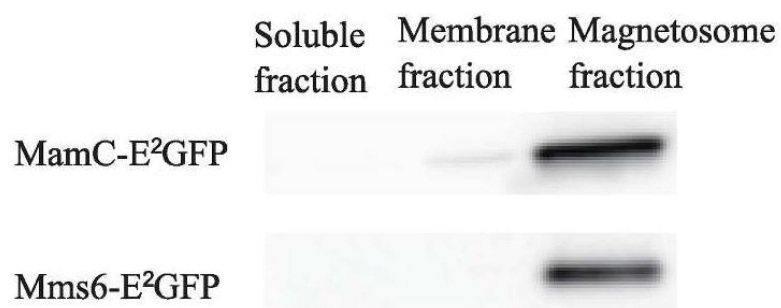
Fig. 2-10 Immunoblots of the soluble, membrane, and magnetosome fractions from MamC-E^{2}GFP- and Mms6-E^{2}GFP-expressing cells with anti-GFP antibodies.
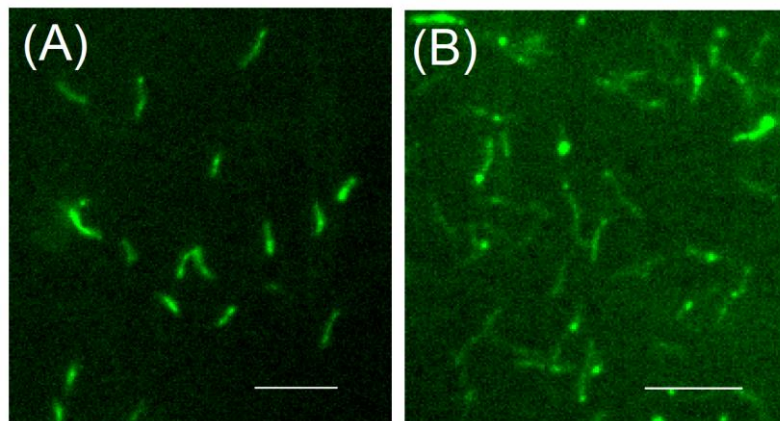
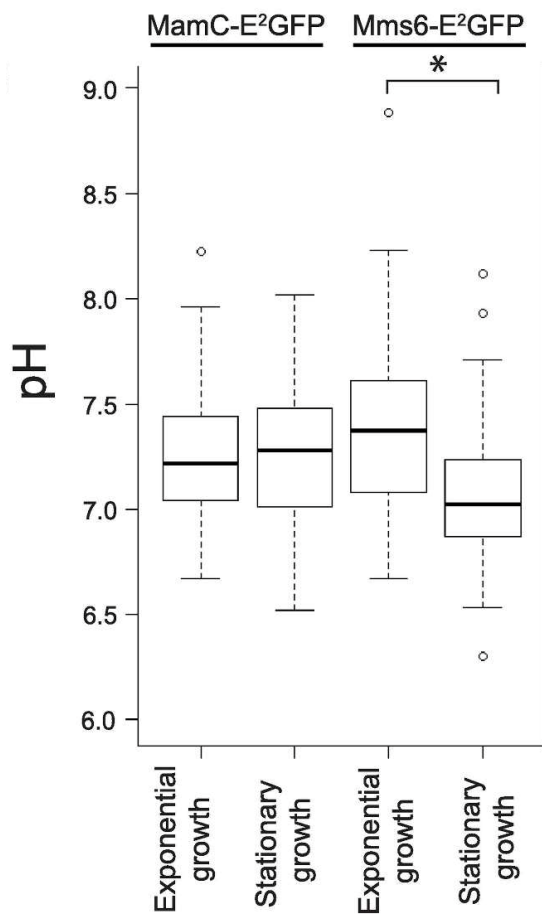Fig. 2-11 Fluorescence microscopic images of Mms6-E^{2}GFP (A) and MamC-E^{2}GFP (B) expressing cells. Bars: 5 μm.

Fig. 2-12 Box plots of pH distributions on the cytoplasmic surface of magnetosome (MamC-E^2GFP) and in the magnetosome lumen (Mms6-E^2GFP) during the exponential and the stationary growth phases. Solid lines indicate the median pH values. The asterisk represents statistical significance in the Mann–Whitney U test ($p < 0.001$).

Chapter III

Heme *c* binding sites of magnetosomal cytochrome MamP are essential for magnetite synthesis

Introduction

According to mutagenesis studies, the *mamAB* operon encoded three putative heme *c* binding proteins, MamE, MamP, and MamT, that were implicated in controlling the crystal size and/or number (Murat et al., 2010; Siponen et al., 2013). Recently, another Mam protein, MamX, has been reported as a putative heme *c* type hemoprotein involved in magnetite biomineralization in MSR-1 (Raschdorf et al., 20113; Yang et al., 2013). These proteins have two putative heme *c* binding motifs (CX_1X_2CH) designated the 'magnetochrome' domain (Siponen et al., 2012). Heme *c* is a molecule involved in transferring electrons, which either reduce or oxidize other molecules. This process is important to MTB because magnetite ($Fe_2O_3 \cdot FeO$) is composed of ferric (Fe^{3+}) and ferrous (Fe^{2+}) ions, so it is necessary to control the redox states of iron during the growth of magnetite crystals. Therefore, these putative magnetosomal hemoproteins could be directly relevant in electron transfer to oxidize or reduce mineral intermediates ferrihydrite such as bacterioferritin or hematite (Staniland et al., 2007; Fdez-Gubieda et al., 2013).

Quinlan et al. showed that MamE from AMB-1 is a bifunctional protein that can localize proteins in the magnetosome and assists in the maturation of small magnetite crystals (Quinlan et al., 2011). They reported that site-directed mutations at both of the putative heme *c* binding motifs in MamE decreased the number of large magnetite crystals in cells, demonstrating that the putative heme *c* binding motifs are involved in biomineralization, especially in the maturation of crystals. Siponen et al. determined the crystal structure of the soluble form of MamP, and demonstrated that MamP is a new type of di-heme *c*-type cytochrome with only 23 residues surrounding the hemes, the smallest heme-binding domain

known thus far (Siponen et al., 2013). Mutational analysis, X-ray crystallography, and biochemical analysis revealed that MamP is an iron oxidase that contributes to the formation of ferrihydrite which is required for magnetite crystal growth *in vivo*.

The focus of my research in this chapter is elucidation of MamP function involved in iron biomineralization. I used immunochemical analyses to confirm that MamP was localized in the membrane fraction of *M. magneticum* AMB-1. Next, I examined the effect of overexpression of wild type MamP and mutant MamP (MamP^{C224A,C268A}) in AMB-1. My results showed that MamP is a membrane-bound *c*-type cytochrome which is localized in the cytoplasmic membrane. Also, the heme *c* binding in MamP is essensial for MamP function in magnetite crystal synthesis.

Materials and methods

Microorganisms and cultures

Bacterial strains and plasmids used in this study are shown in Table 3-1. *M. magneticum* AMB-1 (ATCC 700264) was cultured in chemically defined liquid media under an O_2 (1%) - N_2 (99%) atmosphere at 28˚C and stored in the dark (Blakemore et al., 1979). *Escherichia coli* strains were cultivated in LB broth (Sambrook & Russel, 2001) at 37˚C, if not specified otherwise. When necessary, antibiotics were added at the following concentration: for AMB-1, gentamycin at 5 µg/ml; for *E. coli*, kanamycin at 20 µg/ml, chloramphenicol at 100 µg/ml, and gentamycin at 10 µg/ml. Diaminopimelic acid at 0.3 mM was added to the medium when *E. coli* WM3064 was used as the donor for bi-parental conjugation.

Heterologous expression of MamP in E. coli

For heterologous expression of MamP in *E. coli*, the *mamP* gene was amplified from genomic DNA of *M. magneticum* AMB-1 using primers (forward primer: mamP-infusion_F, 5´- AAGGAGATATACATATGAATAGCAAGGTGGCGCTTCTG-3´; reverse primer: mamP-infusion_R, 5´-GGTGGTGGTGCTCGAGTCACTTTATGACGTGGCAGGCTTC-3´). The amplified DNA fragment was cloned into the pET-29b and digested with NdeI and XhoI using the infusion cloning system (Takara Bio) to create the MamP expression plasmid pET29b-mamP. This plasmid expressed non-tagged MamP protein and it was also used as a template for site directed mutagenesis to create expression plasmids of MamP^{C224A} (pET29b-MamP^{C224A}) (forward primer, mamP_heme1-1: 5'-

GCTATCGCGGCGCCGCCACCGATTGCCACC-3'; reverse primer, R1-1: 5'-CGTGGGGGCGCGGATCGCCCGCCAGGATCA-3') and MamP^{C268A} (pET29b-MamP^{C268A}) (forward primer, mamP_heme2-1: 5'-AAGTGCGCGGGCCGGCCGAAGCCTGCCACG-3'; reverse primer, R2-1: 5'-CGTGAGGATTGACGCTCCGGGCGACCATAT-3'). The plasmid pET-29b-MamP^{C224A} was used as a template for double site-directed mutagenesis to generate expression plasmids of MamP$^{C224A, C268A}$ (pET29b-mamP$^{C224A, C268A}$) using the primer set (mamP_heme2-1 and R2-1). The sequences of these developed plasmids were verified.

Generated plasmids were transformed in *E. coli* C41(DE3) containing pEC86, a plasmid carrying the *ccm* gene cluster, for coexpression of the cytochrome *c* maturation system (Arslan et al., 1998). *E. coli* strains were grown aerobically at 30°C in 200 ml of LB media until an A$_{600nm}$ of 0.6, and then the recombinant proteins were induced with 1 mM isopropyl-β-D-thiogalactopyranoside (IPTG) for 5 h. The cells were harvested by centrifugation at 8,000 × *g* for 15 min. To prepare crude membrane fractions, the cells (ca. 1.5 g in wet weight) were resuspended in 10 mM Tris-HCl (pH 8.0), and disrupted using sonication (130 W for 10 min). The lysate was centrifuged at 8,000 × *g* for 15 min to remove cell debris, then the supernatant was ultracentrifuged at 100,000 × *g* for 60 min. The pellets were suspended in 10 mM Tris-HCl (pH 8.0) and used as the crude membrane fraction.

Overproduction of MamP and MamP mutant in AMB-1

The *mamP* gene and the genes of *mamP*$^{C224A, C268A}$ were cloned into pBBR-tac

(Sakaguchi et al., 2013) using EcoRI and XhoI restriction sites. pBBR-tac was derived from a broad host range plasmid pBBR1 (Antoine & Locht, 1992) harboring the tac promoter, which constitutively expressed the cloned genes. Upon cloning of the *mamP* gene and the mutant genes, ribosome binding sequences 'GGAGAA' were inserted at seven bp upstream of the start codons of each of the genes. The created plasmids were transferred into *M. magneticum* AMB-1 by conjugation from *E. coli* WM3064 as described (Komeili et al., 2004).

Preparation of cellular components

Membrane, soluble, and magnetosome fractions were prepared as previously described (Nguyen et al., 2016).

Immunochemical analyses

Immunoblotting analysis was performed as described (Taoka et al., 2006). Immunoreactivity species of anti- MamP antibodies were detected at a dilution of 1 : 10 000. Goat anti-rabbit IgG conjugated to horseradish peroxidase (GE Healthcare) was diluted 1 : 10,000 using the ECL Plus Western Blotting Detecting Regents (GE Healthcare). The chemifluoresence data were collected using a Luminescent Image Analyzer, LAS 3000 (Fujifilm), and the band intensities were quantified using MULTI GAUGE software version 2.2 (Fujifilm). Immunofluorescence microscopy was performed as previously described (Taoka et al., 2007). The anti-MamP antiserum and preimmuno serum were used at a 1 : 100 dilution, and secondary fluorescein isothiocyanate-conjugated antirabbit immunoglobulin G (EY Laboratories) was used at a 1 : 1500 dilution.

Physical and chemical measurements

The protein concentration was determined using the bicinchoninic acid method (BCA Protein Assay Kit, Pierce Chemical) with BSA as a standard. SDS-PAGE was performed according to the method of Laemmli (Laemmli, 1970). The presence of heme in the gel was detected using heme staining reagents (Connelly et al., 1958). In-gel digestion of protein bands and MALDI-TOF/TOF analysis were performed as described previously (Asano & Nishiuchi, 2011) using the 4800Plus MALDI-TOF/TOFTM Analyzer (Applied Bioscience, Carlsbad, CA), and the results were analyzed using Protein PilotTM software. The redox difference spectra of *E. coli* membrane fractions were obtained using a Shimadzu MPS-2000 spectrophotometer (Shimadzu Corporation), using 1 cm light path cuvettes at room temperature. The membrane fractions were reduced and oxidized by the addition of a small amount of $Na_2S_2O_4$ and $K_3[Fe(CN)_6]$ in the cuvettes, respectively.

Transmission electron microscopy (TEM)

TEM analysis was performed using a JEOL JEM 2000EX TEM operating at 120 kV and a JEOL JEM 2010-FEF TEM operating at 200 kV in bright-field mode. To prepare the specimen for TEM observation, formvar and carbon-coated grids were placed on a drop of cell suspension for 10 min, and directly imaged without staining by TEM. The size of the magnetite crystals was measured using Motic Images Plus 2.3S software v. 2.3.0 (Shimadzu Rika Corporation).

Results

Membrane-bound cytochrome MamP

The amino acid sequences of MamP proteins have three functional regions, a conserved double magnetochrome domain ($\Psi 1X_{5-9}PHX_{5-9}CXXCHX_{1-2}\Psi_2$) (Siponen et al., 2013), a PDZ domain that mediates protein-protein interactions (Ivarsson, 2012), and one predicted transmembrane helix at the N-terminal region (Fig. 3-1). Therefore, based on its amino acid sequence, MamP is predicted to be a membrane anchored c-type cytochrome.

The predicted N-terminal transmembrane region was absent from the MamP crystal structure, because the crystal structure of MamP was determined from the soluble portion of MamP (Siponen et al., 2013). To ascertain whether MamP is a membrane bound c-type cytochrome, I heterogeneously expressed the entire length of MamP from AMB-1 within *E. coli*. It was reported that the coexpression of the *ccm* (cytochrome *c* maturation) genes, together with a structural gene for apocytochrome *c*, can lead to an increase in c-type holocytochrome yields (Arslan et al., 1998). Therefore, the *mamP* gene and *ccm* genes were co-expressed in *E. coli* from pET29b-mamP and pEC86, respectively. The MamP protein was identified as a 32-kDa protein band in membrane fraction by tandem mass spectrometry analysis from the gel of SDS-PAGE (Fig. 3-2 A). Furthermore, this 32-kDa protein band was positively stained using heme staining (Fig. 3-2 B). MamP was highly expressed only in the membrane fraction of *E. coli* (Fig. 3-3). Moreover, according to the difference spectrum analyses, the absorption peaks at 550 nm and 522 nm were observed from the membrane fraction of MamP expressing *E. coli*, but not from the vector control (Fig. 3-4). This spectral

property corresponded to the *alpha* and *beta* absorption peaks of *c*-type cytochromes. On the other hand, the protein band of MamP$^{C224A,\ C268A}$, the MamP mutant for both of heme *c* binding motifs, was not stained by heme staining (Fig. 3-2 B). Furthermore, the absorption peaks at 550 nm and 522 nm were not observed from the membrane fraction expressing the MamP$^{C224A,\ C268A}$ (Fig. 3-4), indicating that MamP is a membrane-bound *c*-type cytochrome.

MamP is localized in cytoplasmic membrane

According to immunoblotting analysis with anti-MamP antibodies, a dense protein band with a molecular mass of 32-kDa was detected from the AMB-1 cell extract (Fig. 3-5). Immunoblotting with an excess amount of MamP did not detect the 32-kDa band, showing that the cross-reaction with MamP was specific (Fig. 3-5). Interestingly, the MamP band was not detected in the magnetosome fraction but in the nonmagnetic membrane fraction (Fig. 3-6). In addition, overproduction of MamP in AMB-1 under the tac promoter using the pBBR-tac plasmid (Sakaguchi et al., 2013) had no effect on MamP localization (Fig. 3-6). According to Immunofluorescence microscopy of MamP-overproduced cells, MamP localized the periphery of the cells (Fig. 3-7), while very low signals were detected in the negative control experiment using the preimmuno serum (Fig. 3-7). These results indicated that MamP localized in the cytoplasmic membrane.

Heme c-binding motifs are necessary for the growth of magnetite crystals during the exponential growth phase

To assess heme *c* binding motifs are necessary for magnetite biomineralization, MamP$^{C224A,\ C268A}$ was overproduced in AMB-1. According to immunoblotting, the content of

the *mamP$^{C224A,\ C268A}$* gene product in MamP$^{C224A,\ C268A}$ overproduced AMB-1 was same as that of wild type MamP overproduced AMB-1 (Fig. 3-8). When wild type MamP was overproduced in AMB-1 cells, the number of magnetite crystals was significantly increased during the exponential phase. Whereas, MamP$^{C224A,\ C268A}$ overproduction resulted in significant decreasing in the number of magnetite crystals (P < 0.001, t-test) (Fig. 3-9, Table 3-2). These results indicated that the *c*-type hemes are necessary for the function of MamP in magnetite biomineralization. Moreover, MamP$^{C224A,\ C268A}$ overproduction affected on magnetite crystal size. MamP$^{C224A,\ C268A}$ overproduced cells mineralized smaller crystals than wild type cells (Fig. 3-10, Table 3-2). The average size of magnetite crystals generated in the MamP$^{C224A,\ C268A}$ overproduced cells was 15.9 ± 7.3 nm (n = 512). There was no crystal with a diameter greater than 45 nm in MamP$^{C224A,\ C268A}$ overproduced cells, whereas 18% of the crystals in wild type cells were larger than 45 nm in diameter (25.6 ± 13.6 nm, n = 677) (Fig. 3-10, Table 3-2).

Discussion

It is important for MTB to control the environment surrounding the magnetite crystals during the mineralization process. This is accomplished by forming specialized vesicles (magnetosomes), which allow the bacteria to form a micro-environment to nucleate and grow crystals while also controlling the crystals' morphology. A key function of this micro-environment is to strictly control the ratio of Fe^{2+}/Fe^{3+} to create mixed-valent crystals of magnetite. Therefore, iron redox proteins localized on the magnetosome membrane are vital for the mineralization process.

In this study, I showed that the highly conserved, magnetosome-associated protein MamP, is a membrane bound c-type cytochrome. To assess the function of this cytochrome on magnetite biomineralization, I overexpressed the native MamP protein and the mutated MamP protein (lacking the two heme c binding motifs) in wild type AMB-1 cells. When the *mamP*$^{C224A, C268A}$ gene was overexpressed from plasmids, the native MamP was probably outcompeted by the MamP$^{C224A, C268A}$, because the overexpression of native MamP had no effect on the size of magnetite crystals (Table 3-2), while MamP$^{C224A, C268A}$ overproduction caused poor crystal growth (Fig. 3-10, Table 3-2). On the other hand, the number of magnetite crystals was the same as those in wild type cells without any plasmid (Fig. 3-9, Table 3-2), therefore, MamP is not likely involved in crystal nucleation, but rather it is involved in the growth of magnetite crystals. The effect of over production of MamP$^{C224A, C268A}$, which lacked heme *c*, on magnetite crystals was similar to the phenotype of the cells lacking the *mamP* gene and that of the mutated MamP protein that lacked the conserved acidic pocket which forms the iron binding site essential for MamP activity (Siponen et al., 2013).

64

Therefore, the heme c within MamP is necessary for growth of magnetite crystal.

Magnetite is a mixture of both iron redox states (ferrous and ferric ions), therefore, redox proteins should be involved in the biomineralization process to control the ratio of ferrous and ferric ions in magnetosome vesicles. Previously, only MamE, P, and T were predicted to be involved in the electron transport process for crystallization, but recently, there have been several reports published about newly discovered electron transport proteins and their involvement in magnetite biomineralization. For example, MamX, conserved in MTB belonging to the alpha proteobacteria, also has the paired magnetochrome domain. Neither the deletion mutants of the entire *mamX* gene nor elimination of its heme *c*-binding magnetochrome domains showed WT-like magnetite crystals. These were flanked within the magnetosome chains by poorly crystalline flake-like particles partly consisting of hematite, indicating that the heme *c* binding motifs of MamX are essential for robust magnetite synthesis (Raschdorf et al., 2013; Yang et al., 2013). Raschdorf et al. also showed that MamZ, which is assumed to be a heme *b* binding YedZ-type ferric reductase, is also involved in magnetite biomineralization (Raschdorf et al., 2013). Moreover, it was also reported that the terminal reductases in denitrification, a respiration process to reduce nitrate to nitrogen or nitrous oxide gas ($NO_3^- \rightarrow NO_2^- \rightarrow NO \rightarrow N_2O \rightarrow N_2$), such as cytochrome cd_1 type nitrite reductase (NirS) (Yoshimatsu et al., 1995; Li et al., 2013) and periplasmic nitrate reductase (Nap) (Taoka et al., 20003; Li et al., 2012), are involved in the redox control of magnetite biomineralization. Because these respiratory enzymes are located on the periplasmic face of the cytoplasmic membrane, the electron transfer pathway is necessary between the cytoplasmic membrane and the magnetosome membrane. Likewise, proteins

possessing a magnetochrome domain may play a role in the electron transport pathway for magnetite biomineralization associated with magnetosome membranes. Because MamP and MamE have a PDZ domain that mediate protein-protein interactions, magnetochrome proteins may form large protein complexes that function as either iron oxidases that provide iron sources for magnetite growth, or function as electron transfer proteins for iron oxidation in magnetosomes. A number of proteins associated with the redox control for magnetite crystallization have been proposed, but further study is needed to clarify the detailed electron transfer pathway for magnetite biomineralization in magnetosomes.

References

Antoine R, Locht C. (1992) Isolation and molecular characterization of a novel broad-host-range plasmid from *Bordetella bronchiseptica* with sequence similarities to plasmids from Gram-positive organisms. *Mol Microbiol*. 6:1785-1799.

Arslan E, Schulz H, Zufferey R, Künzler P, Thöny-Meyer L. (1998) Overproduction of the *Bradyrhizobium japonicum c*-type cytochrome subunits of the cbb_3 oxidase in *Escherichia coli*. *Biochem Biophys Res Commun*. 251:744-747.

Asano T, Nishiuchi T. (2011) Comparative analysis of phosphoprotein expression using 2D-DIGE. *Meth Mol Biol*. 744:225-233.

Blakemore RP, Maratea D, Wolfe RS. (1979) Isolation and pure culture of a freshwater magnetic spirillum in chemically defined medium. *J Bacteriol*. 140:720-729.

Connelly JL, Morrison M, Stotz E. (1958) Hemins of beef heart muscle. *J Biol Chem*. 233:743-747.

Fdez-Gubieda ML, Muela A, Alonso J, García-Prieto A, Olivi L, Fernández-Pacheco R, Barandiarán JM. (2013) Magnetite biomineralization in *Magnetospirillum gryphiswaldense*: time-resolved magnetic and structural studies. *ACS Nano*. 7:3297-3305.

Ivarsson Y. (2012) Plasticity of PDZ domains in ligand recognition and signaling. *FEBS letters*. 586:2638-2647.

Komeili A, Vali H, Beveridge TJ, Newman DK. (2004) Magnetosome vesicles are present

before magnetite formation, and MamA is required for their activation. *Proc Natl Acad Sci USA*. 101:3839-3844.

Laemmli UK. (1970) Cleavage of structural proteins during the assembly of the head of bacteriophage T4. *Nature*. 227:680-685.

Li Y, Bali S, Borg S, Katzmann E, Ferguson SJ, Schüler D. (2013) Cytochrome cd_1 Nitrite Reductase NirS Is Involved in Anaerobic Magnetite Biomineralization in *Magnetospirillum gryphiswaldense* and Requires NirN for Proper d_1 Heme Assembly. *J Bacteriol*. 195:4297-4309.

Li Y, Katzmann E, Borg S, Schüler D. (2012) The periplasmic nitrate reductase Nap is required for anaerobic growth and involved in redox control of magnetite biomineralization in *Magnetospirillum gryphiswaldense*. *J Bacteriol*. 194:4847-4856.

Miroux B, Walker JE. (1996) Over-production of proteins in Escherichia coli: mutant hosts that allow synthesis of some membrane proteins and globular proteins at high levels. *J Mol Biol*. 260:289-298.

Murat D, Quinlan A, Vali H, Komeili A. (2010) Comprehensive genetic dissection of the magnetosome gene island reveals the step-wise assembly of a prokaryotic organelle. *Proc Nat. Acad Sci USA* 107:5593-5598.

Nguyen HV, Suzuki E, Oestreicher Z, Minamide H, Endoh H, Fukumori Y, Taoka A. (2016) A protein-protein interaction in magnetosomes: TPR protein MamA interacts with an Mms6 protein. *Biochem Biophys Rep*. 7:39-44.

Quinlan A, Murat D, Vali H, Komeili A. (2011) The HtrA/DegP family protease MamE is a bifunctional protein with roles in magnetosome protein localization and magnetite biomineralization. *Mol Microbiol*. 80:1075-1087.

Raschdorf O, Müller FD, Pósfai M, Plitzko JM, Schüler D. (2013) The magnetosome proteins MamX, MamZ and MamH are involved in redox control of magnetite biomineralization in *Magnetospirillum gryphiswaldense*. *Mol Microbiol*. 89:872-886.

Sakaguchi S, Taoka A, Fukumori Y. (2013) Analysis of magnetotactic behavior by swimming assay. *Biosci Biotechnol Biochem* 77:940-947.

Sambrook J, Russell DW. (2001) Molecular Cloning: A Laboratory Manual Cold Spring Harbor Laboratory.

Siponen MI, Adryanczyk G, Ginet N, Arnoux P, Pignol D. (2012) Magnetochrome: a *c*-type cytochrome domain specific to magnetotatic bacteria. *Biochem Soc Trans*. 40:1319-1323.

Siponen MI, Legrand P, Widdrat M, Jones SR, Zhang WJ, Chang MC, Faivre D, Arnoux P, Pignol D. (2013) Structural insight into magnetochrome-mediated magnetite biomineralization. *Nature*. 502:681–684.

Staniland S, Ward B, Harrison A, van der Laan G, Telling N. (2007) Rapid magnetosome formation shown by real-time x-ray magnetic circular dichroism. *Proc Natl Acad Sci USA*. 104:19524-19528.

Taoka A, Asada R, Wu LF, Fukumori Y. (2007) Polymerization of the actin-like protein MamK, which is associated with magnetosomes. *J Bacteriol*. 189:8737-8740.

Taoka A, Yoshimatsu K, Kanemori M, Fukumori Y. (2003) Nitrate reductase from the magnetotactic bacterium *Magnetospirillum magnetotacticum* MS-1: purification and sequence analyses. *Can J Microbiol*. 49:197-206.

Yang J, Li S, Huang X, Li J, Li L, Pan Y, Li Y. (2013) MamX encoded by the mamXY operon is involved in control of magnetosome maturation in *Magnetospirillum gryphiswaldense* MSR-1. *BMC Microbiol*. 13:203.

Yoshimatsu K, Fujiwara T, Fukumori Y. (1995) Purification, primary structure, and evolution of cytochrome *c*-550 from the magnetic bacterium, *Magnetospirillum magnetotacticum*. *Arch Microbiol*. 163:400-406.

Tables

Table 3-1. Bacterial stains and plasmid used in this study

Strains or plasmids	Relevant characteristic(s)	Reference or source
Escherichia coli		
XL-1 blue MRF'□	□(*mcr*A)183□□□(*mcr*CB-*hsd*SMR-*mrr*)173 *end*A1 *sup*E44 *thi*-1 *rec*A1 *gry*A96 *rel*A1 *lac* [F',*pro*AB,laqI^{q}Z□□□ M15, Tn10(Tet^R)]	Stratagene
C41(DE3)	F- *ompT hsdS$_B$ (r$_B$-* m$_B$-) *gal dcm* (DE3)	Miroux & Walker (1996)
WM3064	*thrB1*004 *pro thi rpsL hsdS lacZΔM15* RP4-1360 Δ(*araBAD)567 ΔdapA*1341::[*erm pir*]	Demarre et al. (2005)
Plasmids		
pET29b	Protein expression vector for *E. coli*; T7 lac promoter, Kan^r	Novagen
pET29b-mamP	pET-29b carrying *mamP* from *M. magneticum* AMB-1	This study
pET29b-mamP^{C224A,C268A}	pET-29b carrying *mamP*^{C224A,C268A} from AMB-1	This study
pET29b-mamP-His	pET-29b carrying *mamP* from *M. magnetotacticum* MS-1	This study
pEC86	plasmid expressing *ccm* genes from *E. coli*, pACYC184 derivatives, Cm^r	Arslan et al. (1998)
pBBR-tac	Protein expression vector for *M. magneticum* AMB-1, Tac promoter, Mob, Gm^R	Sakaguchi et al. (2013)
pBBR-tac-mamP	pBBR-tac carrying *mamP*	This study
pBBR-tac-mamP^{C224A,C268A}	pBBR-tac carrying *mamP*^{C224A,C268A}	This study

Table 3-2. Effects of MamP expression in magnetite crystals at exponential growth phase (24 h after inoculation)

Strains	Number of crystals in a cell (n = 100)	Crystal size (nm) [1]
Wild type	11.7 ± 4.7	25.6 ± 13.6 (n = 677)
MamP overproduction	18.7 ± 4.7	25.8 ± 14.5 (n = 695)
MamP$^{C224A, C268A}$ overproduction	13.3 ± 4.9	15.9 ± 7.3 (n = 512)

[1] The particle size of the crystal was determined as the average value of the short axis plus the long axis.

Figures
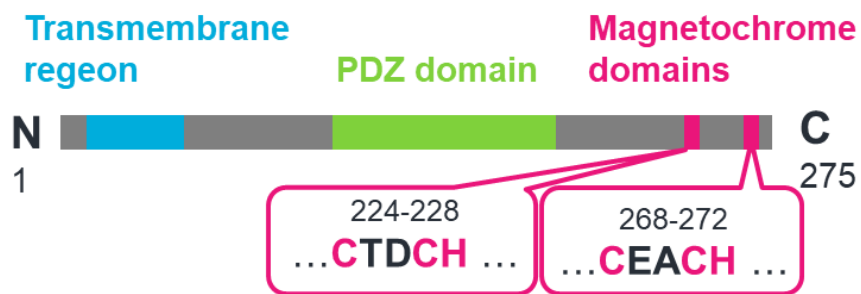
Fig. 3-1 The schematic primary sequence of MamP. MamP have a transmembrane region, a PDZ domain and double magnetochrome domains (Ψ $1X_{5-9}PHX_{5-9}CXXCHX_{1-2}\Psi_2$, Ψ: hydrophobic residues) which contain heme c binding motifs (CX_1X_2CH).
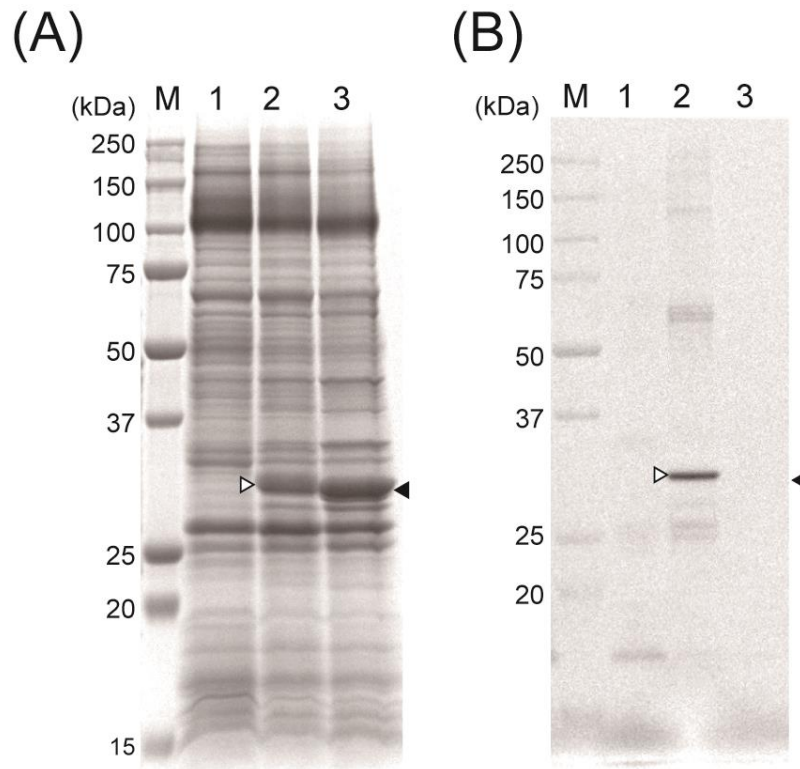
Fig. 3-2 (A) SDS-PAGE gel profiles of the proteins extracted from *E. coli* membrane fractions prepared from vector control strain C41(DE3) (pET29b, pEC86) (lane 1), MamP-expressed strain C41(DE3) (pET29b-mamP, pEC86) (lane 2), and MamP[C224A, C268A]-expressed strain C41(DE3) (pET29b-mamP[C224A, C268A], pEC86) (lane 3). The open triangles and closed triangles indicate the protein band of native MamP and MamP[C224A, C268A], respectively. Each lane contained 40 ɥg of protein, and Coomassie brilliant blue G-250 was used for staining the gel. (B) Heme-stained SDS-PAGE gel for the same samples as the panel (A). Each lane was loaded with 10 ɥg of protein. The molecular masses of the standards (Precision Plus protein standards; Bio-Rad) are indicated on the left sides of the lanes.
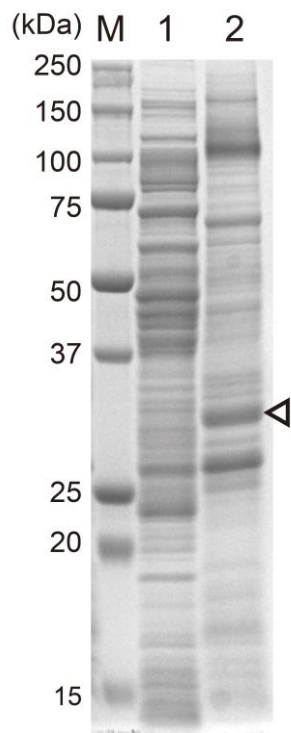
Fig. 3-3 SDS-PAGE gel profiles of soluble fraction (lane 1) and membrane fractions (lane 2) obtained from *E. coli* C41(DE3)(pET29b-mamP). Identified MamP band is represented as the open triangle. Coomassie brilliant blue G-250 was used for staining the gel. The molecular masses of the standards (Precision Plus protein standards; Bio-Rad) are indicated on the left sides of the lanes.
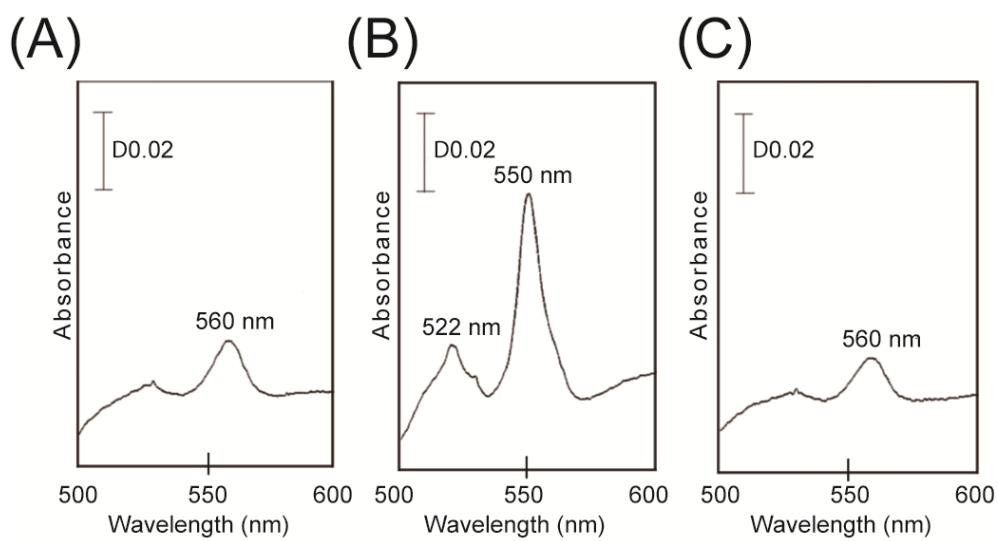
Fig. 3-4 The difference spectra of membrane fractions (one reduced with $Na_2S_2O_4$, one oxidized with $K_3Fe(CN)_6$, then subtracted) obtained from C41(DE3) (pET29b, pEC86) (A), C41(DE3) (pET29b-mamP, pEC86) (B), and C41(DE3) (pET29b-mamP$^{C224A, C268A}$, pEC86) (C).
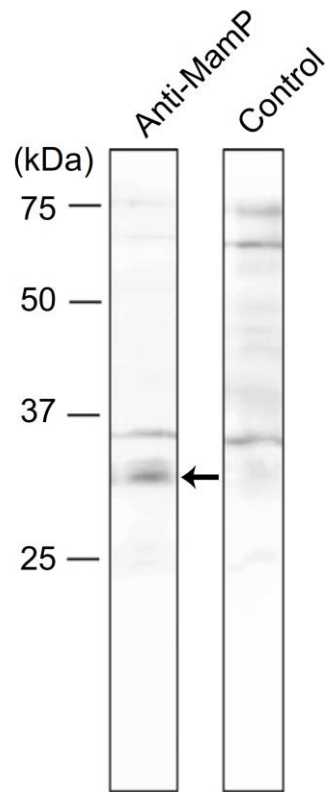
Fig. 3-5 Immunoblot of *Magnetospirillum magneticum* AMB-1 cell extracts using anti-

MamP polyclonal antibodies (left). For the control experiment, the immunoblot was

performed with excess amount (2.3ɥg / mL) of MamP antigen (right). The arrow indicates

the protein band with apparent molecular mass of 32-kDa, which show specific reactivity to

MamP polyclonal antibodies.
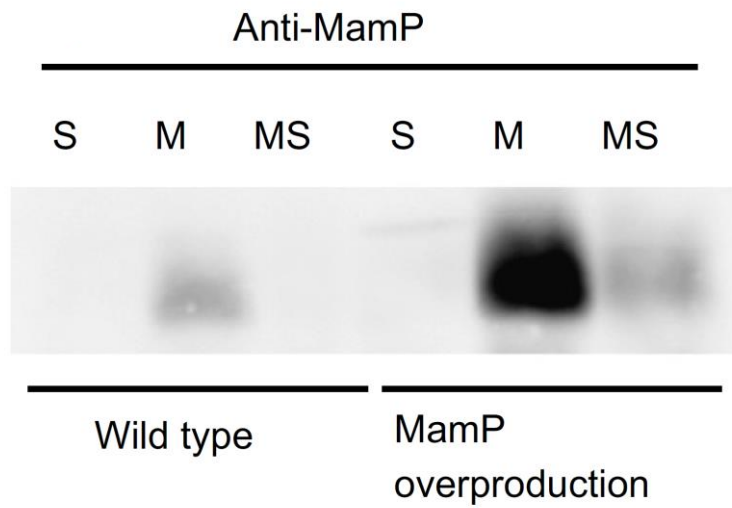
Fig. 3-6 Localization of MamP in WT AMB-1 and MamP-overproduced AMB-1.
Immunoblotting of proteins (20 ɥg/lane) extracted from the soluble fraction (lane S),
membrane fraction (lane M), and purified magnetosome (lane MS) labeled with anti-
MamP.
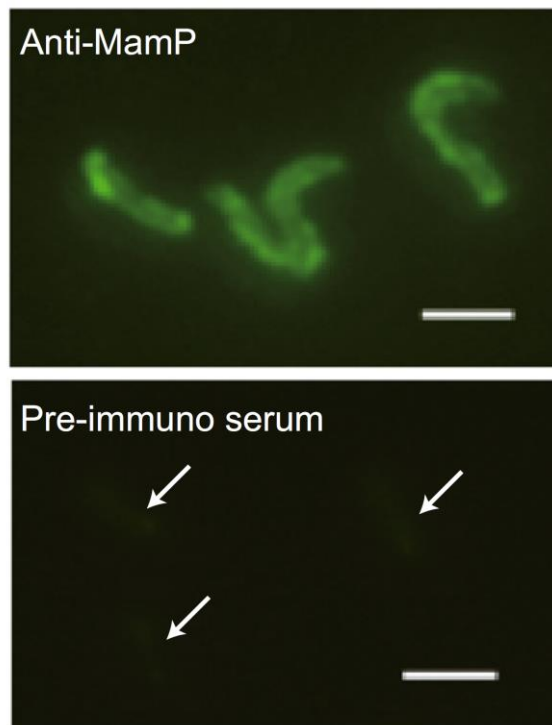
Fig. 3-7 Immunofluorescence microscopic images of MamP-overproduced AMB-1 cells using anti-MamP (top) and preimmuno serum as the negative control (bottom), showing that MamP localized in the peripheral region of the cells. The positions of cells are indicated by white arrows. Scale bars: 2 ųm.
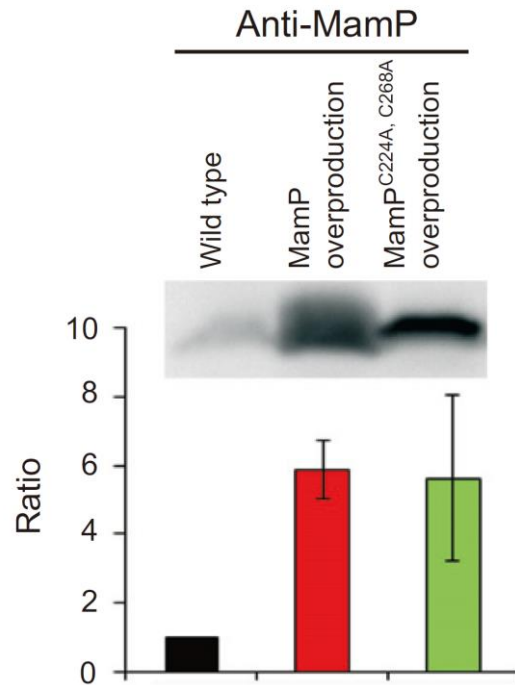
Fig. 3-8 Immunoblot using the anti-MamP antibody of WT, MamP-overproduced, and MamP$^{C224A, C268A}$-overproduced cell extracts (Top). All cell extracts were prepared from cells harvested at 24 h after inoculation. Each lane contained the same amount of protein. Ratio of MamP band intensity analyzed after immunoblotting (Bottom). The band intensity of WT AMB-1 was defined as 1. Values are the averages from three independent cultures.
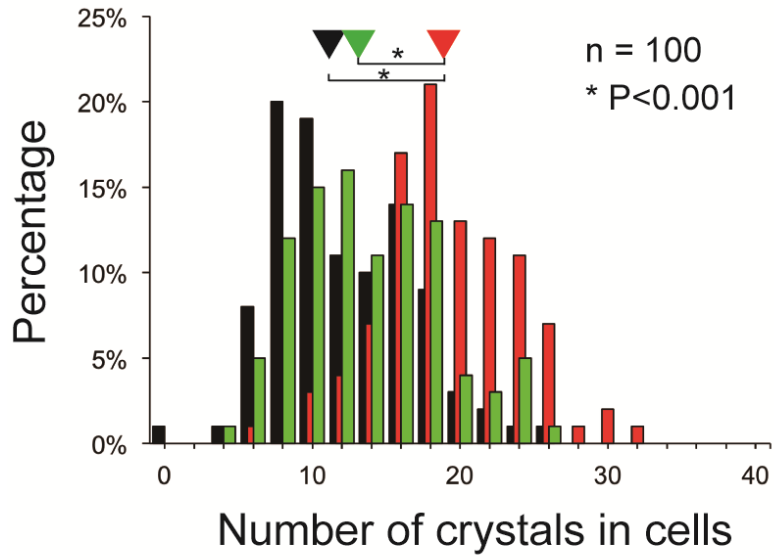
Fig. 3-9 Histogram of the number of magnetite crystals in WT (black bars), MamP (red basr)-, and MamP$^{C224A, C268A}$ (green bars)-overproduced cells at exponential phase (24 h after inoculation). Asterisks represent the statistical significance in the t-test.
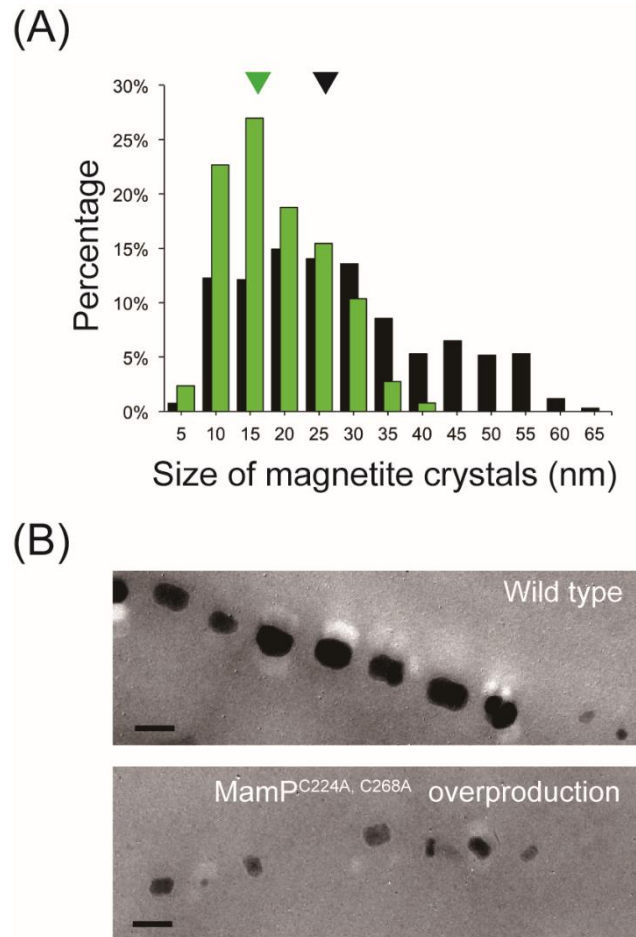
Fig. 3-10 (A) Histogram of magnetite crystal size from WT (black bar) and MamP[C224A, C268A] (green bar)-overproduced cells. Crystal size was defined as the mean value of the long axis and the short axis. Triangles represent the average values in crystal size. (B) TEM micrographs of WT (top) and MamP[C224A, C268A]-overproduced (bottom) cells 24 h after inoculation. Scale bars: 50 nm.

Acknowledgements